JℳPAPERS

Global modes of viscous heated jets with real gas effects

S. Demange[1],†, U.A. Qadri[2], M.P. Juniper[2] and F. Pinna[1]

[1]Department of Aeronautics and Aerospace, von Kármán Institute, Rhode-Saint-Genese 1640, Belgium

[2]Department of Engineering, University of Cambridge, Cambridge CB2 1PZ, UK

This study investigates the stability features of spatially spreading heated jets in the viscous regime with real gas effects, using both unsteady two-dimensional axisymmetric simulations and linear analyses of the steady state and time-averaged states. At a Reynolds number of 400, the heated jets are found to undergo a subcritical Hopf bifurcation, marking the start of self-sustained oscillations when decreasing the temperature ratio $S = T_\infty/T_c$, which highly depends on the thermodynamic and transport property assumptions imposed in the simulations. Once the flow enters a limit cycle past the Hopf bifurcation, the linear analyses over the steady base state are unable to capture the oscillation's frequency. Nevertheless, this study confirms that including real gas effects in the stability equations has a strong effect on the growth rate of the global mode once the centreline temperature of the jet reaches that of the dissociation reaction onset, which is $T = 2800\,\mathrm{K}$ for air at $p_s = 100\,\mathrm{mbar}$. The linear global analyses over the time-averaged states lead to a satisfying prediction of the oscillation's frequency for the cases studied, and the baroclinic torque obtained from the resulting global mode matches well with that of the simulations.

Key words: jets, bifurcation, Absolute/convection instability

1. Motivations

At sufficiently high Reynolds numbers, low-density jets undergo a Hopf bifurcation once their centreline-to-ambient density ratio S_ρ is below a critical value $S_{\rho,H}$. This bifurcation marks the beginning of the self-sustained production of periodic vorticity waves and enhanced mixing. This has been observed experimentally by Monkewitz *et al.* (1990) in heated jets and by Kyle & Sreenivasan (1993) for light jets, where density variations are caused by the injection of a lighter gas into an ambient heavier gas. The occurrence of self-sustained perturbations was first correlated to the presence of an absolute instability

† Email address for correspondence: simon.demange@vki.ac.be

pocket in the jet, using the local linear stability theory and assuming quasi-parallel flows (Huerre & Monkewitz 1985; Monkewitz & Sohn 1998).

Since these initial studies, several analyses have been devoted to the understanding of the mechanisms behind the convective-to-absolute instability transition, and the influence of flow parameters on it. The role of the Mach and Reynolds' numbers, as well as the azimuthal wavenumber m, were investigated by Jendoubi & Strykowski (1994), Sevilla, Gordillo & Martínnez-Bazan (2002), Lesshafft & Huerre (2007), Balestra, Gloor & Kleiser (2015) among others. As an important result, Lesshafft & Huerre (2007) identified the leading role of the baroclinic torque in the formation of absolute instabilities. Further analyses showed that absolute instabilities were particularly sensitive to the precise shapes of the base flow profiles (Coenen, Sevilla & Sanchez 2008; Lesshafft & Marquet 2010; Coenen & Sevilla 2012), while the consequence of confinement was studied by Juniper (2006, 2008) for round and planar jets and wakes.

In recent years, the increase of available computational resources has allowed the quasi-parallel flow assumption to be relaxed in stability analyses, using the so-called BiGlobal analysis (Theofilis 2003). Modelling low-density jets with the Navier–Stokes equations and applying BiGlobal analysis lead to the identification of an isolated mode in the global spectra (Qadri, Chandler & Juniper 2015; Coenen *et al.* 2017; Qadri, Chandler & Juniper 2018) corresponding to the single-frequency periodic oscillations observed in experiments. This numerical analysis leads to an accurate numerical quantification of the bifurcation parameters and oscillation frequencies. Similar analyses were recently developed to include the influence of buoyancy in round and planar light jets (Bharadwaj & Das 2017, 2019), as well as in thermal plumes (Chakravarthy, Lesshafft & Huerre 2018).

However, these results from the BiGlobal or local absolute instability theory are obtained in cases where the non-normality of the global linear operator is weak. As shown by Chomaz (2005), in some cases and especially for weakly non-parallel flows, a strong non-normality of the linear operator may lead to transient growth phenomena and overall sensitivity of the spectrum to perturbations, able to destabilize the flow away from the linear instability threshold. In such cases, a transient nonlinear analysis is then required.

Most of the above heated jet analyses assume that the gas is calorically perfect with uniform specific heats c_p and c_v, and has uniform transport properties, such as viscosity and thermal conductivity (Lesshafft & Huerre 2007; Lesshafft *et al.* 2015; Chakravarthy *et al.* 2018). In contrast, light jets analyses often consider a viscosity law based on the different species' mass fractions (Coenen & Sevilla 2012; Bharadwaj & Das 2017; Coenen *et al.* 2017; Bharadwaj & Das 2019). Once the centreline temperature of heated jets is high enough, however, the calorically perfect gas (CPG) assumption breaks down (Anderson 2006) and the local stability features are observed to be sensitive to changes of the thermodynamic and transport property (TTP) modelling for highly viscous regimes (Demange & Pinna 2020). High-enthalpy jets can be found in many industrial and research applications, from coating processes (Spores & Pfender 1989) and medical applications (Kolb *et al.* 2008), to high-enthalpy facilities for research on atmospheric entry applications (Marieua *et al.* 2007; Cipullo *et al.* 2014). In high-enthalpy wind tunnels the prediction of bifurcation parameters is paramount, because globally unstable jets have a reduced stable potential core and increased entrainment of the surrounding cold gas towards the centreline, which adversely affect the measurements made in these facilities. Furthermore, the accurate estimation of the global mode frequency is essential to identify the origin of the hydrodynamic behaviour in more realistic cases in which external disturbances are present (Cipullo *et al.* 2014).

The objective of this study is therefore to analyse the stability features of spatially spreading heated jets in the viscous regime, with an emphasis towards high-enthalpy configurations for which centreline temperatures exceed those of most previous studies. In this paper typical flow conditions and TTP models from plasma wind tunnel operations (Demange, Chazot & Pinna 2020) are investigated (low *Re*, *M* and static pressure), while retaining well-known jet profile shapes from the literature. The analysis is restricted to the axisymmetric framework, as previous experimental (Sreenivasan, Raghu & Kyle 1989; Monkewitz & Sohn 1998; Hallberg & Strykowski 2006) and numerical analyses (Lesshafft & Huerre 2007; Coenen & Sevilla 2012) have shown that axisymmetric perturbations dominate the stability behaviour of low-density jets for the parameters studied. The scope of the stability analyses in this work is limited to the linear framework, in line with recent low-density jet analyses (Bharadwaj & Das 2017; Coenen *et al.* 2017; Chakravarthy *et al.* 2018).

This study starts by introducing the methodology followed to obtain the governing equations, flow properties, simulations and stability analysis in § 2. A phenomenological study of unsteady simulations of heated jets is performed in § 3. Features of the hydrodynamic behaviour observed in direct numerical simulation (DNS) are then compared against results from linear analysis on the steady states in § 4, and from BiGlobal analysis on time-averaged states in § 5.

2. Problem and model description

This study investigates the hydrodynamic behaviour of axisymmetric heated round jets, formed by the injection of a heated gas at temperature T_c into the same ambient gas at a lower temperature $T_\infty = 350$ K. In this context, $S = T_\infty/T_c$ defines a temperature ratio, rather than the density ratio S_ρ often found in studies concerned with light jets (Coenen *et al.* 2008; Bharadwaj & Das 2017; Coenen *et al.* 2017; Bharadwaj & Das 2019). No buoyancy forces are considered because the Grashoff number of the heated jets remains low $Gr\ O(10^{-5})$. The axisymmetric geometry is described with cylindrical coordinates: $\boldsymbol{x} = r\boldsymbol{e_r} + \theta\boldsymbol{e_\theta} + z\boldsymbol{e_z}$, respectively defining the radial, azimuthal and streamwise directions. The symmetry axis is aligned with the streamwise direction $\boldsymbol{e_z}$. The fluid investigated is air, and is described by its velocity components $\boldsymbol{u} = u\boldsymbol{e_r} + v\boldsymbol{e_\theta} + w\boldsymbol{e_z}$, density ρ, temperature T, static enthalpy h, viscosity μ, thermal conductivity κ and pressure p, all of which vary in space.

The spatio-temporal evolution is governed by the compressible Navier–Stokes equations, given in their non-dimensional form as

$$\frac{\mathrm{D}\rho}{\mathrm{D}t} + \rho\,(\boldsymbol{\nabla} \cdot \boldsymbol{u}) = 0, \tag{2.1a}$$

$$\rho\frac{\mathrm{D}\boldsymbol{u}}{\mathrm{D}t} = -\boldsymbol{\nabla}p + \frac{1}{Re}\boldsymbol{\nabla} \cdot \tau, \tag{2.1b}$$

$$\rho\frac{\mathrm{D}h}{\mathrm{D}t} = Ec\frac{\mathrm{D}p}{\mathrm{D}t} + \frac{Ec}{Re}\,(\boldsymbol{\nabla} \cdot (\tau\boldsymbol{u}) - \boldsymbol{u}\boldsymbol{\nabla} \cdot \tau) + \frac{1}{Pr \cdot Re}\boldsymbol{\nabla} \cdot (\kappa\boldsymbol{\nabla}T)\,, \tag{2.1c}$$

where τ is the viscous stress tensor

$$\tau = \mu(\boldsymbol{\nabla}\boldsymbol{u} + \boldsymbol{\nabla}\boldsymbol{u}^{\mathrm{T}} - \tfrac{2}{3}\,(\boldsymbol{\nabla} \cdot \boldsymbol{u})\,\boldsymbol{I}), \tag{2.2}$$

and quantities are non-dimensionalized with respect to their inlet centreline values ($r = 0$, $z = 0$), labelled '$\cdot_c$', with the exception of the reference pressure, which is set to $\rho_c w_c^2$. When enforcing the parallel flow assumption for local stability analyses, quantities are

Flow assumption	Primary variables	Secondary variables
CPG	$\boldsymbol{u}, T, p$	ρ, μ, κ, h or c_p
LTE	$\boldsymbol{u}, T, p$	$\rho, \mu, \kappa, h, \zeta, F, G, H_m$

Table 1. List of the primary/secondary variables chosen to describe the flow. The H_m, F and G quantities are grouping terms introduced by Malik & Anderson (1991) for high-enthalpy flows, while ζ is the compressibility factor from (2.7).

scaled with respect to their local centreline values ($r = 0$). The reference length is set to the jet's radius R, yielding the flow's characteristic time $\tau_{flow} = R/w_c$. Consequently, the main non-dimensional numbers in (2.1a) to (2.1c) are

$$Re = \frac{\rho_c w_c R}{\mu_c}, \quad Ec = \frac{w_c^2}{h_c}, \quad M = \frac{w_c}{a_c}, \quad Pr = \frac{\mu_c h_c}{\kappa_c T_c}, \quad (2.3a\text{--}d)$$

where a_c is the inlet centreline speed of sound defined as $a_c = \sqrt{\gamma \mathcal{R} T_c}$, with γ the heat capacity ratio and $\mathcal{R}$ the specific gas constant. In (2.1c) the Eckert number Ec is preferred to the Mach number M, because it agrees better with the notion of equilibrium flow presented in § 2.1.2. For a CPG, $Ec = (\gamma - 1)M^2$ is retrieved.

2.1. *Property models*

In order to define the thermodynamic and transport properties of the fluid forming the heated jet, a distinction between primary and secondary flow quantities is introduced. The former represents the minimum set of quantities used to describe the flow, while the term property model is used to define the ensemble of relations used to obtain the secondary quantities from primary thermodynamic quantities. The lists of primary/secondary quantities depend on the thermodynamic and chemical assumptions of the flow, and are summarized in table 1.

The relations between primary and secondary quantities are expected to influence the stability features of the flow through two means: (i) indirectly, by influencing the distribution of primary quantities through transport phenomena in the governing equations; (ii) directly through secondary quantities' base state values and perturbation's expansion in the stability equations (see Appendix A.1).

Similarly to a previous study (Demange & Pinna 2020), two main thermodynamic and chemical assumptions are considered in order to model the flow. The first considers air to be a single CPG with no chemical activity, as in most of the literature on heated jet instabilities (Lesshafft & Huerre 2007; Balestra *et al.* 2015; Chakravarthy *et al.* 2018). The second stems from high-enthalpy flow literature (Anderson 2006) and uses a mixture of calorically perfect species allowing for dissociation reactions and vibrational excitation. Both assumptions are detailed below.

2.1.1. *Single species CPG*

By definition, the CPG assumption relies on a constant isobaric specific heat $c_p = 1004$, $5 \, \text{J} \, \text{kg}^{-1} \, \text{K}^{-1}$ (for air), linearly relating the temperature to the static enthalpy: $h = c_p T$. Furthermore, the Prandtl number is imposed to be constant, and set to a common value for diatomic gases $Pr = 0.7$. As a single air species is considered, the density is expressed
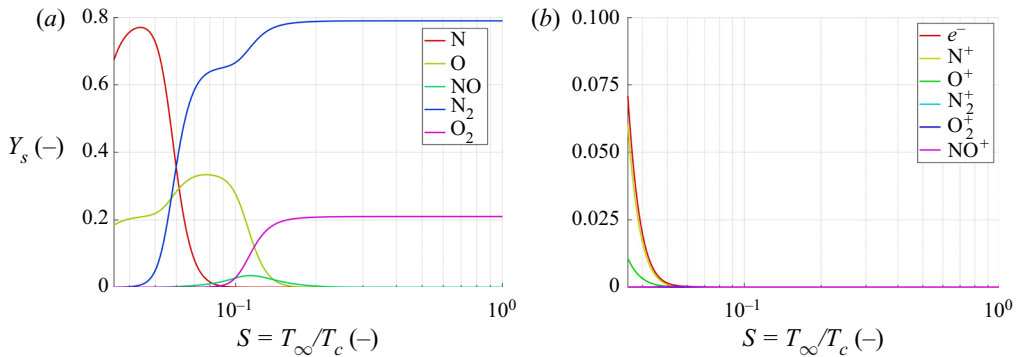
Figure 1. Concentration of the 11-species composing the air mixture from Park (1993) with respect to the temperature ratio $S = T_\infty/T_c$, assuming $T_\infty = 350\,\mathrm{K}$ and pressure $p_s = 100\,\mathrm{mbar}$: (*a*) shows the neutral species; (*b*) shows the charged species.

through the state equation

$$\rho = pT\gamma M^2. \tag{2.4}$$

While performing simulations and stability analyses, the influence of transport phenomena on the hydrodynamic features of the jets is investigated by considering the following two formulations of the viscosity and thermal conductivity.

(i) The CPG-CP model assumes constant transport properties: $\mu = cst$ and $\kappa = cst$, which is commonly found in stability analyses of low-density jets (Lesshafft & Huerre 2007; Balestra 2013; Chakravarthy *et al.* 2018) but is a rough approximation in the viscous regime (Demange & Pinna 2020).

(ii) The CPG-VP model assumes temperature-dependent transport properties. The viscosity is obtained from Sutherland's law (Sutherland 1893)

$$\mu = \mu_{ref} + \left(\frac{T}{T_{ref}}\right)^{3/2} \frac{T_{ref} + S_{su}}{T + S_{su}}, \tag{2.5}$$

where $\mu_{ref} = 1789 \times 10^{-5}\,\mathrm{kg\,m^{-1}\,s^{-1}}$, $T_{ref} = 288\,\mathrm{K}$ and $S_{su} = 110\,\mathrm{K}$. While the thermal conductivity is obtained from $\kappa = \mu c_p Pr^{-1}$.

2.1.2. *Equilibrium mixture of gases (LTE)*

When increasing the temperature of a gas (at constant pressure), the CPG assumption fails due to the excitation of different energy modes (rotational, vibrational and electronic) and the rise of chemical processes (Anderson 2006). Therefore, a more accurate model considers the air as a mixture '$\mathcal{S}$' of calorically perfect species 's', with a fixed elemental composition and volume percentages of 21 % O_2 and 79 % N_2. The composition of the gas and chemical reactions accounted for correspond to the 'air-11' mixture from Park (1993). The same mixture was used in a previous study (Demange *et al.* 2020), and the corresponding concentrations $Y_s = \rho_s/\rho$ are plotted in figure 1. Thus, the density of the mixture is defined as

$$\rho = \sum_{s\in\mathcal{S}} \rho_s. \tag{2.6}$$
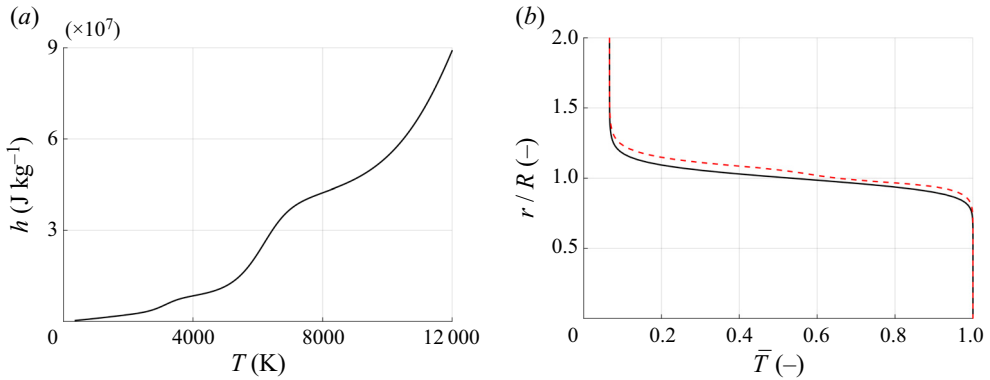
(a)

(b)

Figure 2. (a) Nonlinear relation between the mixture's static enthalpy and the temperature in LTE with $p_s = 100$ mbar; resulting LTE inlet formulations imposing either a top-hat profile of temperature (LTE-T ——) or static enthalpy (LTE-h - - -) for $S = 0.0667$.

Furthermore, we assume that the characteristic times needed for the chemical reactions and energy modes to reach an equilibrium state are negligible compared with the flow's characteristic time τ_{flow}. Consequently, the mixture is said to be in local thermodynamic and chemical equilibrium, abbreviated here to 'LTE'. This implies that, for a given temperature and pressure, the mixture composition $Y_s(T, p)$ is fully determined, and that a single temperature is needed to describe the flow. The governing equations are then completed by the mixture state equation given as

$$H_m p = \rho T \zeta, \tag{2.7}$$

where $\zeta = \mathcal{M}_{undiss}/\mathcal{M}$ is the compressibility factor obtained from the mixture's molar mass $\mathcal{M}$ and $\mathcal{M}_{undiss} = 0,21\mathcal{M}_{O_2} + 0,79\mathcal{M}_{N_2}$, and $H_m = u_c^2/(T_c \mathcal{R})$ is a grouping term introduced by Malik & Anderson (1991). This form of the state equation implies that $T_\infty/T_c \neq \rho_c/\rho_\infty$ at constant pressure, unlike with the CPG assumption.

Species thermodynamic properties are obtained similarly to Miró Miró *et al.* (2019), assuming them to behave as a rigid rotor and harmonic oscillator. The mixture's enthalpy is then obtained from

$$h = \sum_{s \in \mathcal{S}} Y_s h_s. \tag{2.8}$$

The resulting nonlinear relation between the static enthalpy and the temperature is illustrated in figure 2. Transport properties $\mu(T, p)$ and $\kappa(T, p)$ are computed from approximations of the Chapman and Enskog gas theory, while barodiffusion and elemental demixing are ignored (Miró Miró *et al.* 2019).

2.2. *Unsteady simulations and steady states*

Simulations of the heated jets are performed to obtain both the steady state solutions $\bar{q} = [\bar{u}, \bar{T}, \bar{p}]$ used in the stability analysis, and the unsteady evolution of the flow $q(x, t)$. To this end, an existing DNS code (Nichols 2005; Chandler *et al.* 2012; Qadri *et al.* 2015, 2018) is used, which solves the low Mach number approximation of the axisymmetric Navier–Stokes equations. This formulation effectively splits the pressure into a slow thermodynamic component $p^{(0)}$, assumed constant, and a fast hydrodynamic component $p^{(1)}$, which is the solution to a Poisson equation. The resulting equations allow for

S	0.4	0.3	0.222	0.2	0.1667	0.1429	0.125	0.111	0.1	0.0667
Re_D			400							
R/θ			20							

Table 2. Inlet parameters chosen for the simulations of synthetic heated jet flows in this study, θ indicates the shear-layer momentum thickness. In the case of the CPG-CP flow, an additional simulation is performed at $S = 0.0909$.

density variations due to temperature gradients, while neglecting those associated with the pressure.

The 'top-hat' distributions of temperature and velocity (number 2 from Michalke 1984) are imposed at the domain's inlet ($z = 0$), while varying the temperature ratio in the range $S \in [0.0667; 0.4]$. Values of S and other inlet parameters studied are given in table 2. The choice of Reynolds' number is based on typical values found at the inlet of the VKI Plasmatron plasma jet (Demange *et al.* 2020), while the shear-layer thickness is given a middle value from ranges studied in the literature (Lesshafft & Huerre 2007). A co-flow of 1 % of the centreline velocity is also injected to improve numerical stability. Remaining boundary conditions mimic a semi-infinite domain allowing for gas entrainment on the lateral sides of the domain (Nichols, Schmid & Riley 2007; Chandler *et al.* 2012). The domain studied extends to respectively [0; 30] and [−5; 5] diameters ($D = 2R$) in the streamwise and radial directions. In unsteady simulations a non-dimensional time step of $\Delta t = 0.005$ is imposed after initializing the flow by copying the inlet profiles through the domain. Unlike the analysis of Lesshafft, Huerre & Sagaut (2007), no perturbation is injected in the flow because the initialization procedure was found to be enough to trigger self-sustained oscillations.

Steady solutions are obtained using a selective frequency damping method introduced by Åkervik *et al.* (2006) and implemented by Chandler *et al.* (2012) in the DNS. Simulations are considered as converged once residuals reach 10^{-6}, and examples of steady states are plotted in figure 3. Both steady/unsteady simulations use the same mesh with (713; 513) grid points along the (e_z; e_r) directions.

The different flow models presented in § 2.1 are implemented in the DNS code, which originally considered only CPG flows with constant transport properties. Modifications of the DNS code for the CPG-VP model are straightforward, while details of the LTE implementation are given below.

2.2.1. *High-enthalpy jet simulations*

When considering the flow as an equilibrium mixture, the low Mach number framework is replaced by a low Eckert number expansion of the Navier–Stokes equations, which leads to a similar system of non-dimensional equations

$$\frac{\partial \rho^{(0)}}{\partial t} + \nabla(\rho u)^{(0)} = 0, \tag{2.9a}$$

$$\frac{\partial(\rho u)}{\partial t} + \nabla(\rho u u) = \nabla p^{(1)} - \frac{S_\rho}{Re_D}\nabla(\tau), \tag{2.9b}$$

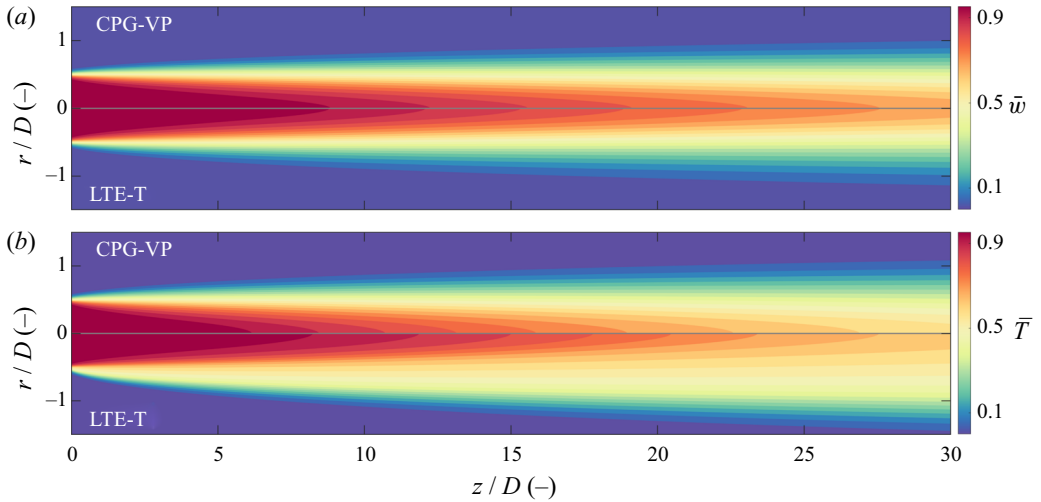$$\rho\frac{\mathrm{D}h}{\mathrm{D}t} = \frac{S_\rho}{Re_D Pr_2}\nabla(\lambda\nabla T), \tag{2.9c}$$

Figure 3. Examples of the heated jets steady streamwise velocity (*a*) and temperature (*b*) for $S = 0.0667$, $Re_D = 400$ and $R/\theta = 20$ with the CPG-VP and LTE-T flow models.

where the reference quantities are chosen at the inlet centreline, with the exception of the reference density ρ_∞ which is taken in the outer flow and the reference static enthalpy $h_{ref} = p_\infty/\rho_\infty (= h_\infty - e_\infty)$, where e_∞ is the internal energy in the outer flow. The resulting non-dimensional numbers are defined as

$$S_\rho = \frac{\rho_c}{\rho_\infty}, \quad Re_D = \frac{\rho_c u_c D}{\mu_c}, \quad Ec_2 = \frac{\rho_\infty u_c^2}{p_\infty} \quad \text{and} \quad Pr_2 = \frac{\mu_c}{\kappa_c T_c} \frac{p_\infty}{\rho_\infty}. \quad (2.10a\text{–}d)$$

As flow properties depend on the pressure p in LTE, a low static pressure of $p_s = 100$ mbar is prescribed, which is representative of plasma wind tunnel conditions where the LTE assumption was validated experimentally (Cipullo 2010). Although the value of p_s is fairly low, the continuum flow assumption is still valid because the Knudsen number of the flow remained below 0.01 for all cases.

Based on the nonlinear relation relating the static enthalpy to temperature in LTE (see figure 2*a*), two formulations of the inlet energy condition are compared against each other in this study (see figure 2*b*).

(i) The LTE-h model imposes a top-hat profile of static enthalpy at the inlet. For each value of S, an equivalent enthalpy ratio h_∞/h_c is obtained and an equivalent temperature inlet profile is retrieved by inverting the enthalpy-temperature relation.
(ii) The LTE-T model imposes a top-hat profile of temperature at the inlet, similarly to the energy condition of the CPG models.

We emphasize that both conditions are not equivalent for the same value of S, because the LTE-h inlet condition yields a temperature layer slightly shifted outward of the shear layer, with humps due to dissociation relations (Demange & Pinna 2020). The LTE-h model also introduces slightly more thermal energy in the flow than the LTE-T one. Details of the numerical implementation of the LTE model are given in Demange, Qadri & Pinna (2019). Finally, we also stress that based on the current definition of the Reynolds number, the mass flow injected into the simulations is modified by the CPG or LTE assumption imposed on the flow. In practice, the LTE assumption results in an increased inlet mass flow with respect to its CPG counterpart, in particular at low S.

936 A7-8

2.3. *Linear stability analyses*

The analysis of the jets' stability features is carried out within the classical linear framework, decomposing flow quantities into the sum of a base state value and small non-interacting axisymmetric perturbations: $q(\boldsymbol{x}, t) = \bar{q}(\boldsymbol{x}) + \varepsilon q'(\boldsymbol{x}, t)$ with $\varepsilon \ll 1$. Perturbations take the shape of normal modes of the flow by performing a Fourier transform in the homogeneous spatial directions of the flow and a Laplace transform in time

$$q'(\boldsymbol{x}, t) = \tilde{q}(\boldsymbol{x}) \, e^{i\phi} + c.c., \tag{2.11}$$

where $\tilde{q}$ is the complex shape function, ϕ is the complex phase function and '*c.c.*' denotes the complex conjugate needed for q' to be a real quantity.

In the following, both the local and BiGlobal approaches are considered. Within the local formulation, one must ensure a separation of scales between the development length of the flow $\mathcal{L}_{flow}$ and typical perturbation wavelengths (section 3 in Huerre & Monkewitz 1990), allowing perturbations to take a wave-like form in the $\boldsymbol{e}_z$ and $\boldsymbol{e}_\theta$ directions, with a phase function given by (2.12*a*). For the BiGlobal analysis, the flow is considered homogeneous only along the azimuthal direction, leading to the so-called global modes (Theofilis 2003) with a phase function given by (2.12*b*). In the phase functions

$$\phi = \alpha z - \omega t, \tag{2.12a}$$

$$\phi = -\omega t, \tag{2.12b}$$

α denotes the streamwise wavenumber and ω the complex angular frequency.

Once completed with the boundary conditions of Appendix A.2, the stability equations are obtained by introducing the linear ansatz and modal perturbations into the compressible Navier–Stokes equations (2.1). Finally, the generalized eigenvalue problem of the form

$$(\underline{\underline{A}} + \underline{\underline{B}}\omega)\tilde{q} = 0 \tag{2.13}$$

is retrieved, where $\underline{\underline{B}}$ is the matrix containing terms multiplying ω, $\underline{\underline{A}}$ contains the remaining terms including α and $\tilde{q}$ is the eigenvector array associated with the eigenvalue ω. Matrices $\underline{\underline{A}}$ and $\underline{\underline{B}}$ are detailed in a previous study (Demange & Pinna 2020) for the local problem, and in the supplementary materials of this paper for the BiGlobal problem available at https://doi.org/10.1017/jfm.2022.43. The resulting eigenvalue problems are solved in the VESTA toolkit (Pinna 2013), using a Chebyshev collocation method for the local problem, and the sixth-order finite difference method from the UEFD Fortran library by Hermanns & Hernández (2008) for the heavier BiGlobal problem.

In order to determine the noise amplifier (globally stable) or self-excited oscillator (globally unstable) nature of the flows (Huerre 2000), the spatio-temporal formulation of the local analysis is used, allowing one-dimensional waves to grow both in space ($\alpha \in \mathbb{C}$) and time ($\omega \in \mathbb{C}$). Following Huerre & Monkewitz (1985), absolute instabilities are found at each streamwise position by examining the sign of the absolute growth-rate $\mathrm{Im}(\omega^*)$, obtained where iso-contours of ω form a valid (Briggs 1964; Bers 1984) saddle point in the complex wavenumber plane ($\partial_{\alpha \in \mathbb{C}} \omega^* = 0$). As summarized by Coenen & Sevilla (2012), the actual transition to a globally unstable flow depends on the position and extent of the resulting absolute region defined by $\sigma(z) \geq 0$ (Chomaz, Huerre & Redekopp 1988; Couairon & Chomaz 1999). Using the BiGlobal approach, the stable/unstable nature of the global (linear) mode is directly given by the growth-rate $\mathrm{Im}(\omega)$ in the phase function of (2.12*b*).

3. Unsteady simulations: the full nonlinear behaviour

Unsteady two-dimensional axisymmetric simulations are performed by letting the flow evolve without forcing after the initialization procedure. In all cases, a transient regime is observed following $t = 0$, during which rolled-up vortices grow in the shear layer shortly after the inlet. Depending on the case studied, the transient regime is followed either by a periodic regime with the self-sustained production of vortical structures, or by a dampening of the transient features and a slow convergence towards the steady state. In the remainder of this paper, the first outcome of the simulations will be labelled as globally unstable, while the second will be referred to as globally stable.

In the globally unstable cases, self-sustained oscillations take the shape of rolled-up vortices appearing within the first 2 diameters downstream of the inlet. This contrasts with the higher Reynolds' number ($Re_D = 7500$) and thicker shear layer ($R/\theta_0 = 10$) simulations of Lesshafft *et al.* (2007), where vortical structures grew approximately 5 to 6 diameters away from the inlet. By comparing the results of Lesshafft *et al.* (2007) against a preliminary simulation with $Re_D = 7500$ and $R/\theta = 20$, it is found that the steady potential core is shorter in our cases due to the thinner shear layer imposed at the inlet, rather than by the different Reynolds number.

Due to the axisymmetric assumption imposed upon the governing equations, vortical structures are allowed to survive for longer than they would in three-dimensional configurations, where they would eventually breakdown. Therefore, the long-time behaviour of vortical structures downstream and outside of the jet should be regarded as non-physical, while in the present case axisymmetric flow features near the inlet remain physically relevant.

3.1. *Onset of self-sustained oscillations*

According to the convective to absolute boundary diagram displayed in figure 4(*a*) from Demange & Pinna (2020), all the inlet conditions defined in table 2 are already absolutely unstable. As detailed in § 4.1, this does not necessarily mean that all conditions studied are globally unstable in the sense of Chomaz (2005). However, the resulting jets are expected to be close to the Hopf bifurcation (Chakravarthy *et al.* 2018), and to experience self-sustained oscillations once the temperature ratio is lowered below a threshold value, S_H (Monkewitz & Sohn 1998; Qadri *et al.* 2015; Coenen *et al.* 2017). A summary of the resulting stable and unstable configurations is given in figure 4(*b*), which shows a strong dependence of the bifurcation and the onset of the periodic regime to the TTP model used to describe the flow.

For non-reacting flows (CPG), different models of the transport properties (μ and κ) have a strong influence on the global stability behaviour. When uniform and constant properties are prescribed (CPG-CP), the jets remain globally stable for most of the conditions studied and the bifurcation is only observed for temperature ratios below $S < 0.1$. This is confirmed by an additional simulation performed with this model for $S = 0.0909$, where the flow is globally unstable. An example of the CPG-CP simulation is provided in the supplementary materials (see movie_1). However, if the temperature-dependent transport properties are taken into account (CPG-VP), the jets undergo a bifurcation to a globally unstable regime as soon as $S \leq 0.2225$.

In the case of chemically reacting flows (LTE), the bifurcation is observed for slightly lower temperature ratios ($S_H = 0.5$) for both types of energy inlet. Given that, for this temperature ratio, Sutherland's law remains accurate and that dissociation reactions are yet to be activated, the bifurcation delay between the LTE and CPG-VP jets is probably
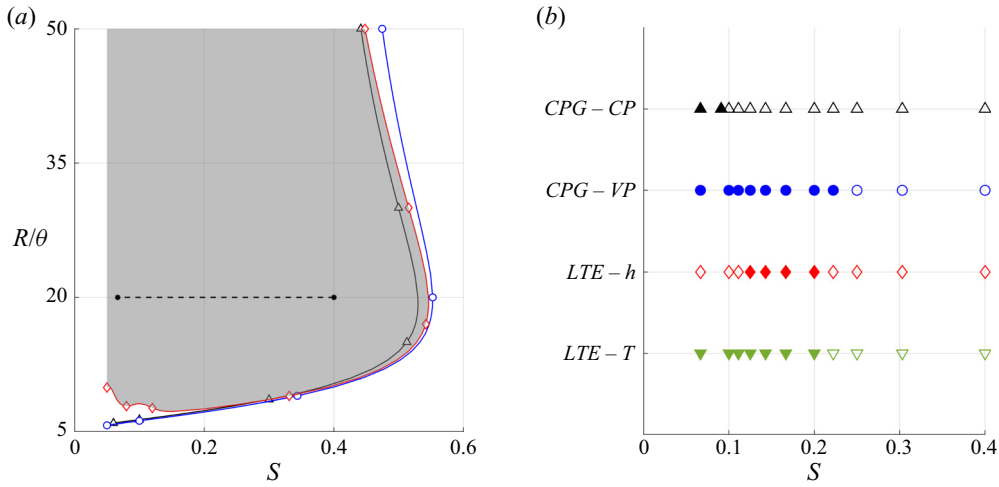
Figure 4. (*a*) Comparison of the inlet conditions chosen for the simulations of the synthetic heated jet (- - -) against the convective-to-absolute instability boundary obtained in a previous study (Demange & Pinna 2020) with the CPG-CP ($\triangle$), CPG-VP ($\circ$) and LTE-h ($\diamond$) models for the one-dimensional inlet profiles (the greyed area denotes an absolutely unstable parallel flow). (*b*) Diagram representing the outcome of unsteady simulations, cases either exhibit self-sustained oscillations (filled symbols) or converge towards a steady state (open symbols).

related to the vibrational excitation (≈ 900 K Anderson 2006), which marks the end of the CPG assumption's validity. Interestingly, a restabilization is observed for the LTE jets with top-hat inlet profiles of static enthalpy (LTE-h) as $S < 0.125$. As this restabilization is not observed with the LTE-T jets, these results confirm the importance of the inlet profiles' shape on the stability features (Coenen & Sevilla 2012).

In a recent study, Zhu, Gupta & Li (2017) proposed a criterion to predict the parameters of Hopf bifurcations in low-density jets, based on experimental and numerical results. It is worth mentioning that most of the low-density jets studied by Zhu *et al.* (2017) are in fact light jets, where the density gradient is created by injecting a lighter species (such as helium) into a quiescent heavier gas. However, heated jets are known to present different profiles to those of light jets (Coenen & Sevilla 2012), thus altering the stability properties. Using the formula from Zhu *et al.* (2017), bifurcation parameters can be related through

$$S_{\rho,H}^{-1} = \frac{(Re_D^{-1} - a)}{bD\theta_0^{-1}} + 1, \tag{3.1}$$

where $a = -3.785 \times 10^{-4}$ and $b = 1.019 \times 10^{-5}$. Using the same definition of θ_0 as Zhu *et al.* (2017) and setting $Re_D = 400$ in (3.1), this criterion predicts a value of $S_{\rho,H} = 0.1338$, which is approximately half the value found in our simulations with the CPG-VP model.

3.2. *Behaviour of the globally unstable flows*

Among the globally unstable jets, three types of behaviour are observed depending on the TTP model and value of S imposed. Evidence of these types of behaviour are provided by snapshots of the non-dimensional azimuthal vorticity ($\Omega = \partial_z u - \partial_r w$), and space–time diagrams of radial velocity perturbations in the shear layer $v' = v(z, r=1, t) - \hat{v}(z, r=1)$,
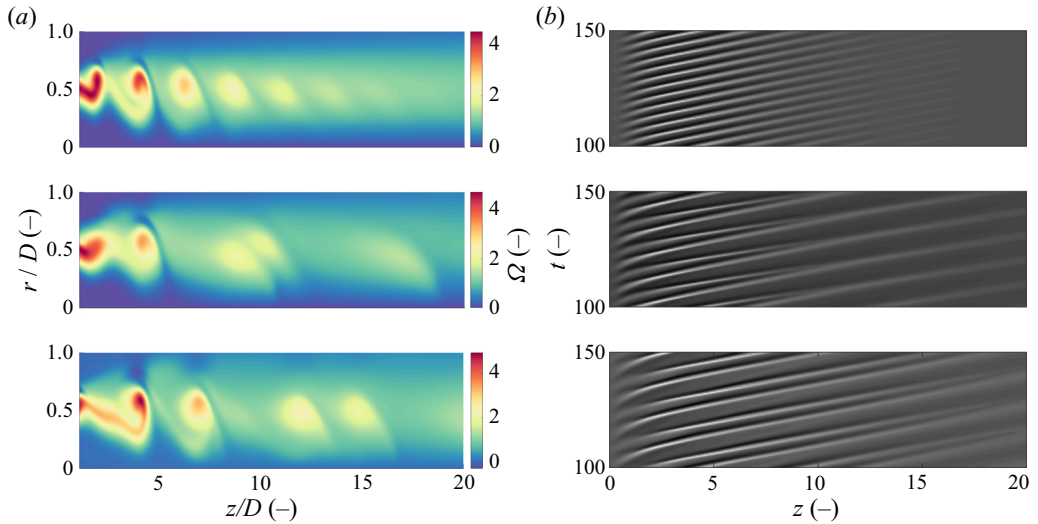
Figure 5. Illustration of the three different behaviours of the unsteady heated jets, here for the LTE-T model at $S = [0.2; 0.111; 0.0667]$ (top to bottom): shown through (*a*) snapshots of the (non-dimensional) vorticity $\Omega = \partial_z u - \partial_r w$; and through (*b*) spatio-temporal diagrams of the radial velocity perturbations $v' = v(z, r = 1, t) - \hat{v}(z, r = 1)$, where $\hat{v}$ is the time-averaged value. Animations of the corresponding vorticity contours are available in the supplementary materials (movie_2a, movie_2b and movie_2c).

where $\hat{v}$ is the time-averaged radial velocity. Both are displayed in figure 5 for cases computed with the LTE-T model, because it is found to display all three behaviours depending on the value of S.

In globally unstable jets with moderate temperature ratios ($S \geq 0.125$), vortices are produced periodically in the shear layer before moving downstream without interacting with each other (see movie2a in supplementary materials). Vortical structures growing near the inlet are then advected downstream while diffusing. A slight movement of their centres towards the jet's centreline is also observed during this process.

When increasing the centreline temperature, periodic vortex coupling events occur after the transient regime for the LTE-T model at $S = [0.1; 0.111]$ (see movie2b in supplementary materials) and the CPG-VP model at $S = 0.0667$. These events consistently remain at a fixed streamwise position, $z_{pair} \approx 10D$ for both LTE cases and $z_{pair} \approx 8D$ for the CPG-VP case. Similar phenomena were also described in simulations by Lesshafft *et al.* (2007) for all their unstable cases with $R/\theta > 10$ and $Re_D = 7500$, and in experiments by Kyle & Sreenivasan (1993) in light jets with thin shear layers and Reynolds number above $Re_D > 2000$. The present observations suggest that the occurrence of these events depends more strongly on the temperature ratio and precise shape of the profiles (imposed by changes of the TTP models) in a highly viscous regime.

Finally, increasing the centreline temperature to even lower temperature ratios ($S = 0.0667$) is found to produce a third type of behaviour only in the case of the LTE-T jets. Vortices are then produced in pairs, and closely follow each other without coupling before the diffusion of these structures renders any observation impracticable (see movie2c in supplementary materials). Although the initial phase is physically accurate, this is not the case during the later phase because these unstable structures would break down more quickly in three-dimensional simulations.
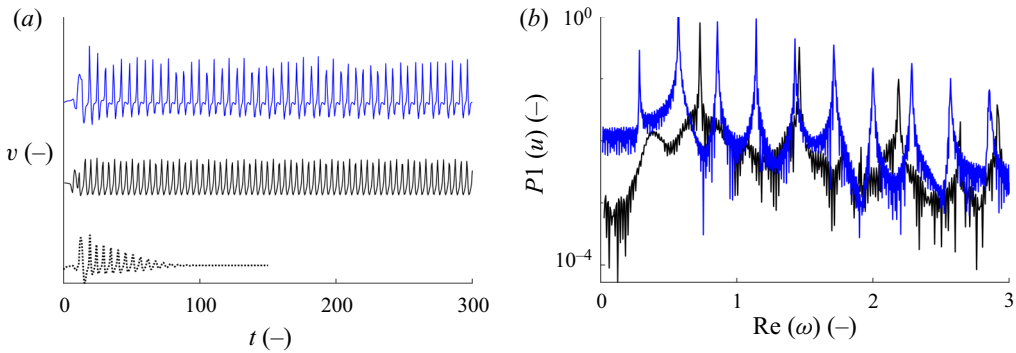
936 A7-12

Figure 6. Time evolution of the radial velocity (*a*) at $(z, r) = (5; 0.5)D$ for the CPG-CP ($\cdots$) flow at $S = 0.1429$, the CPG-VP (black ——) flow at $S = 0.1429$ and the CPG-VP (blue ——) flow with vortex coupling at $S = 0.0667$; FFT spectra (*b*) of the CPG-VP flows at $S = 0.1429$ (black ——) and $S = 0.0667$ (blue ——), ignoring the transient regime.

S	0.222	0.2	0.1667	0.1429	0.125	0.111	0.1	0.0909	0.0667
$\omega_{r,\text{CPG-CP}}$	—	—	—	—	—	—	—	0.515	0.465
$\omega_{r,\text{CPG-VP}}$	0.754	0.767	0.7540	0.729	0.704	0.679	0.654	*	0.569
$\omega_{r,\text{LTE-h}}$	—	0.738	0.723	0.670	0.562	—	—	*	—
$\omega_{r,\text{LTE-T}}$	—	0.762	0.746	0.721	0.675	0.636	0.597	*	0.471

Table 3. Main non-dimensional frequencies obtained from the FFT analysis of unsteady simulations at $z = 5D$ and $r = D/2$ for each globally unstable model, '—' indicates a stable case without periodic regime and '*' an absence of simulation.

3.3. *Frequency content*

Unsteady simulations are also used to extract the frequency of self-sustained oscillations observed in the globally unstable cases. As seen in the time history of the radial velocity fluctuations displayed in figure 6, unstable cases present a remarkably periodic behaviour, in agreement with previous experimental (Monkewitz *et al.* 1990; Hallberg & Strykowski 2006) and numerical (Lesshafft *et al.* 2007) observations. For this figure, the reference time scale is chosen as $t_{ref} = D/w_c$. The frequency of these oscillations is recovered by performing a fast Fourier transform (FFT) analysis in the shear layer, at $(z, r) = (5; 0.5) \times D$, where perturbations are amplified. Examples of the power spectra obtained for unstable cases are also given in figure 6. In the absence of vortex coupling, the spectrum contains the main frequency ω_r and higher harmonics (black spectrum in figure 6). In the cases where vortex coupling is observed (blue spectrum in figure 6), a first sub-harmonic is present on the left of the main peak at $1/2\omega_r$, as well as for higher frequencies ($3/2\omega_r$, $2\omega_r$, $5/2\omega_r$ and so on), similarly to (Monkewitz *et al.* 1990; Lesshafft *et al.* 2007).

The main frequencies of self-sustained oscillations are given by the maximum of power spectra obtained from the FFT analysis for each case and are reported in table 3 in non-dimensional form: $\text{Re}(\omega) = 2\pi Df/w_c$. As seen from these results, the frequency of self-sustained oscillations decreases when the centreline temperature of the jet is increased.

In the following, frequencies from the present study are compared against the universal frequency scaling proposed by Hallberg & Strykowski (2006) for low-density jets.
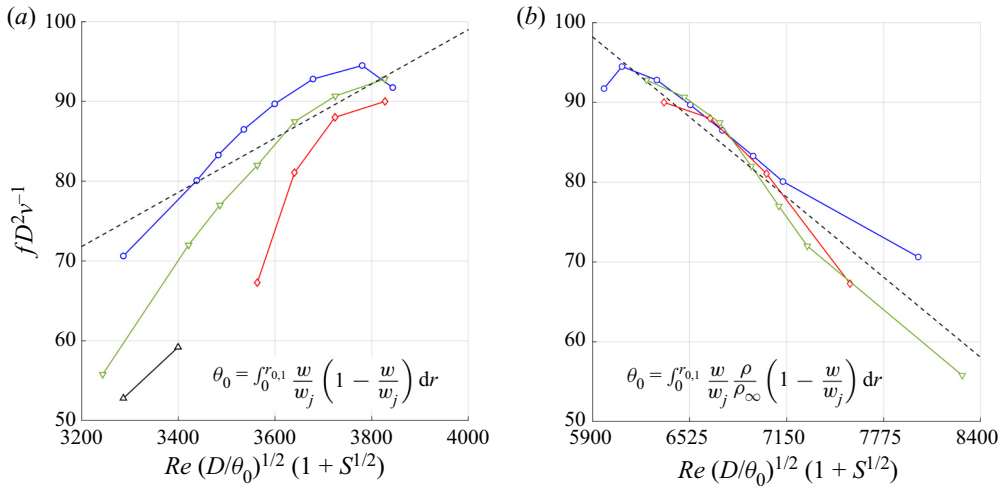
Figure 7. Frequencies obtained from the unsteady DNS using the CPG-CP ($\triangle$), CPG-VP ($\circ$), LTE-h ($\diamond$) and LTE-T ($\triangledown$) TTP models; (*a*) shows the comparison between the present DNS results against the criterion as given by Hallberg & Strykowski (2006); (*b*) shows a similar criterion, this time with the compressible momentum thickness, resulting coefficients are given as $fD\nu^{-1} = 193.1 - 0.01608Re(D/\theta_0)^{1/2}(1 + S^{1/2})$, and lead to a $R^2 = 0.93$ fitness. Note that for this figure only, S is the density ratio.

This criterion estimates the global frequency based on inlet parameters such as the initial momentum thickness $\theta_0 = \int_0^{r_{0.1}} w(r)[1 - w]\,dr$, with $r_{0,1} = r(w = 0.1)$, and viscous scale obtained from the inlet centreline kinematic viscosity $\nu = \mu_c/\rho_c$, while assuming top-hat-like inlet shapes

$$fD^2\nu^{-1} = a + bRe\left(\frac{D}{\theta_0}\right)^{1/2}(1 + S_\rho^{1/2}), \tag{3.2}$$

with coefficients from Hallberg & Strykowski (2006), $a = -37$ and $b = 0.034$. Similarly to the bifurcation criterion of Zhu *et al.* (2017), the reference data of Hallberg & Strykowski (2006) includes mostly light jets results, except for the heated jets of Lesshafft *et al.* (2005), and higher Reynolds numbers.

The comparison of the present simulations' results with different TTP models against the frequency criterion is displayed in figure 7(*a*). Results show that the general trends from our DNS results are in good agreement with the proposed scaling, showing that this criterion can be used as a preliminary estimation for the global frequency of heated jets. However, curves from the different TTP models do not collapse onto each other, and display a shape similar to those obtained with the heated jet data of Lesshafft *et al.* (2005) reported in Hallberg & Strykowski (2006, figure 8). This observation reinforces the argument that heated and light jets have different global stability behaviour, both in their bifurcation and frequency parameters.

Proposing a similar criterion for heated jets lies beyond the scope of the present study. Nonetheless, we note that this frequency scaling partly takes into account differences between the CPG and LTE models through changes of ν for the same values of Re and S, but cannot account for modifications of the thermal layer such as those found when comparing the LTE-h and LTE-T formulations. Therefore, the same criterion is investigated for the variable property models using the compressible definition of the momentum thickness $\theta_0 = \int_0^{r_{0.1}} w\rho[1 - w]\,dr$ in figure 7(*b*). The proposed fit displays a

936 A7-14

reversed orientation of the criterion, with new coefficients $a = 193.1$ and $b = -0.01608$, but an improved linear fitness of $R^2 = 0.93$ with results from the LTE-h and LTE-T flow models collapsing to a common shape.

4. Linear analyses of the steady states

Linear local and BiGlobal stability analyses of the steady states are performed, and their results are compared against features observed with the unsteady simulations from the previous section. In all the following, only axisymmetric instabilities are considered with $m = 0$, as they proved to yield the most unstable modes in all cases.

Initially, an estimation of the bifurcation parameters is obtained from the linear analyses in § 4.1. Then, the role of flow modelling in the trends of global growth rate is discussed in § 4.2. Finally, estimations of the heated jets oscillations frequency from linear analyses on the steady state is investigated in § 4.3.

4.1. *Prediction of the critical temperature ratios*

First, typical results from the local and BiGlobal analyses are given for the $S = 0.111$ case, where the centreline temperature is sufficiently high to bring out the differences between TTP models. Second, the analyses are generalized to the complete range of temperature ratios.

Figure 8(*a*) displays an example of the absolute growth rate along the $\boldsymbol{e}_z$ direction for the $S = 0.111$ jet with each TTP model. Absolute regions start at the inlet and end where $\omega_i^*(z) = 0$, which defines the absolute length l_{ac}. For configurations where the inlet profile is already absolutely unstable, previous nonlinear (Chomaz *et al.* 1988; Couairon & Chomaz 1999) and linear (Coenen & Sevilla 2012) analyses indicate that the occurrence of an unstable global mode depends on the streamwise extent of the absolute region. For the case plotted, the absolute lengths obtained with each TTP model are coherent with the DNS observations: the globally stable CPG-CP and LTE-h jets display shorter absolute regions than the globally unstable CPG-VP and LTE-T jets. Additionally, the perturbations at the inlet displayed in figure 8(*b*) are typical of the jet-column mode observed by Lesshafft & Huerre (2007) for this type of jet. An example of a BiGlobal analysis is then considered.

Figure 9(*a*) displays the BiGlobal spectra obtained with each TTP model for the same $S = 0.111$ case. Similarly to previous BiGlobal analyses of low-density jets (Chakravarthy *et al.* 2018; Qadri *et al.* 2018; Bharadwaj & Das 2019), the spectra include an isolated mode corresponding to the oscillations observed in simulations, and a continuous branch sensitive to the domain's length. In the present study no absorbing layer is added to the eigenvalue problem (EVP) (Lesshafft 2018), because the continuous branches remained stable. Similarly to the local analysis for the same S, BiGlobal results are coherent with the DNS observations: both the CPG-VP and LTE-T jets are linearly globally unstable, while the CPG-CP and LTE-h jets remain stable. This observation reveals both a strong influence of the inlet shapes and TTP modelling over the global stability features of viscous heated jets. The corresponding global mode shapes are given in figure 9(*b*) for each flow model. Perturbations of the stable global modes extend towards the end of the domain, while those of unstable modes have a more compact spatial structure for this case. For both the LTE-T and LTE-h jets, perturbations start closer to the inlet than for the CPG assumptions and are confined to a smaller radial extent. This is believed to be caused by the faster spreading of jets obtained with the LTE transport and thermodynamic properties. Global mode shapes are also compared against that of the local absolute mode with the
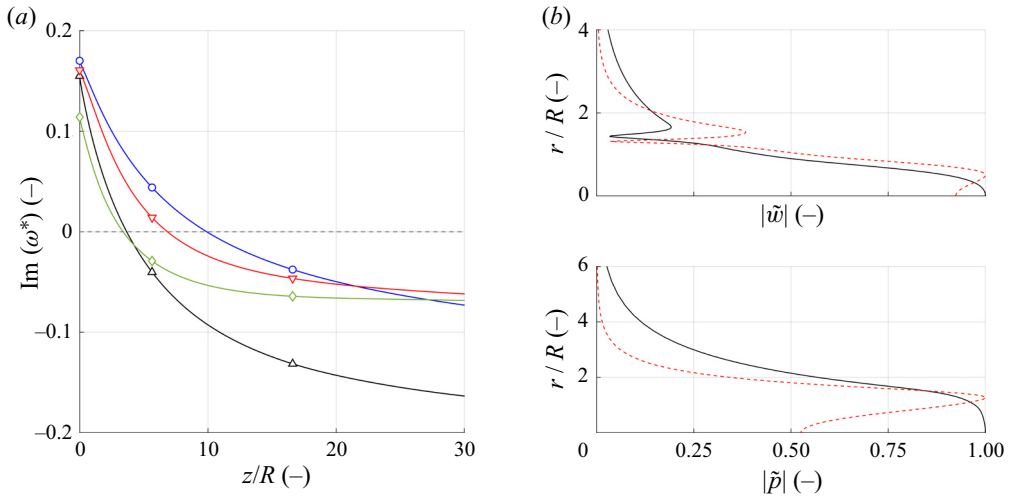
Figure 8. Results from the local linear analysis of the steady heated jets with $S = 0.111$ and the CPG-CP ($\triangle$), CPG-VP ($\circ$), LTE-h ($\diamond$) and LTE-T (∇) flow models: (a) absolute growth rate from the local analysis along the streamwise direction; (b) absolute value of the streamwise velocity (up) and pressure (down) perturbations corresponding to the absolute mode (——) at $z = 5R$, BiGlobal mode perturbations (- - -) for the same case and position are added for comparison (CPG-VP only).
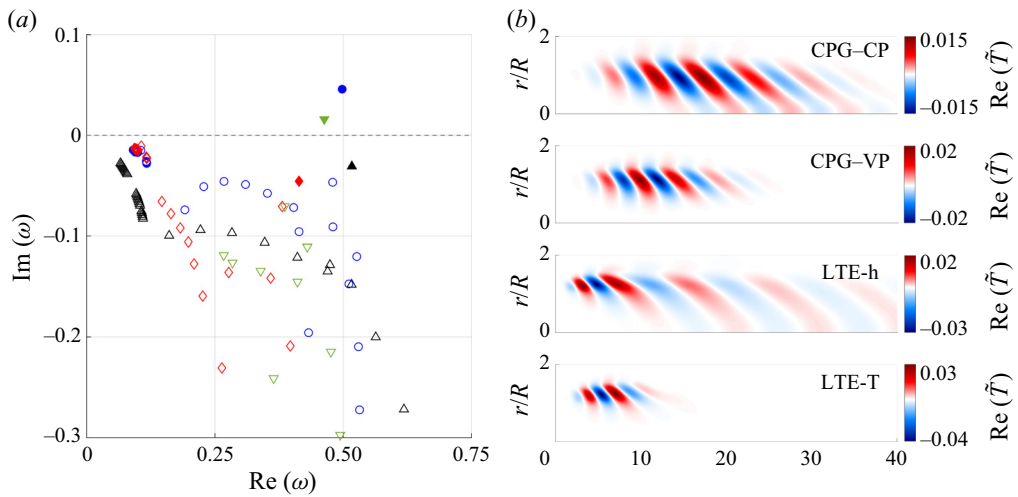
Figure 9. Results from the BiGlobal linear analysis of the heated jets with $S = 0.111$: (a) spectra from the BiGlobal EVP with $m = 0$ for the CPG-CP ($\triangle$), CPG-VP ($\circ$), LTE-h ($\diamond$) and LTE-T (∇) flow models, isolated modes are indicated with filled symbols; (b) real part of BiGlobal isolated mode's temperature perturbations obtained with the different TTP models for the same case.

CPG-VP model in figure 8(b), revealing that both methods yield similar features in the shear layer, but differ towards the centreline of the jet.

Results from the local and global analyses are then generalized to the complete range of temperature ratio S. Starting with the global analysis, the trend of the global growth rate as a function of S are given in figure 10(a) for each of the TTP models. The growth rates obtained with each model are negative for the maximum value of S, and increase with decreasing S. In the case of the LTE-h jet, the growth rate remains negative for the whole
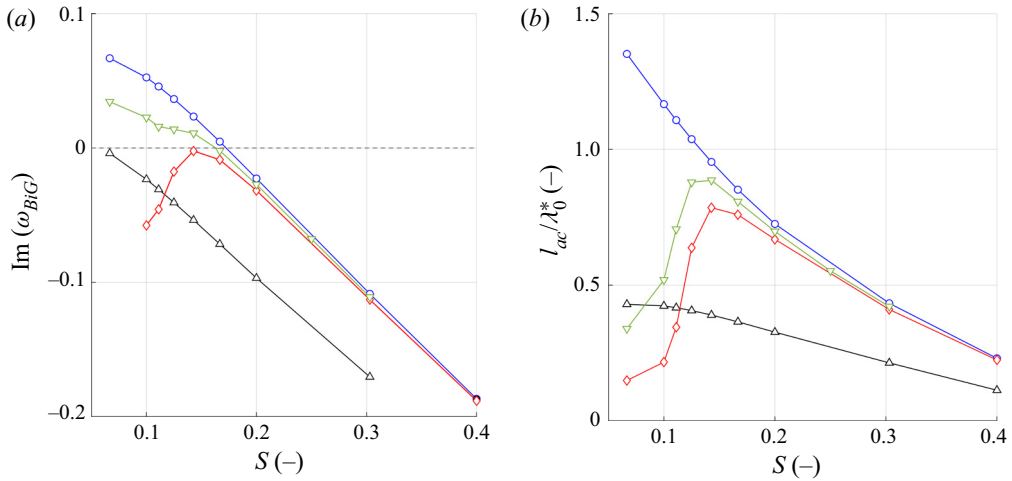
936 A7-16

Figure 10. Generalization of the linear analyses to the full range of S studied with the CPG-CP ($\triangle$), CPG-VP ($\circ$), LTE-h ($\diamond$) and LTE-T ($\triangledown$) flow models: (*a*) BiGlobal growth rates; (*b*) length of the absolute region normalized with the inlet absolute wavelength from local analyses. As a remainder, the CPG-VP jet bifurcates for $S = 0.2222$, the LTE jets at $S = 0.2$ and the LTE-T jet restabilize at $S = 0.1111$.

range of S and reaches a maximum for $S = 0.1429$, and decreases for lower values of S. Despite the apparent mismatch with the simulations where the LTE-h jet does become globally unstable, the trends obtained are coherent with the restabilization observed. For the CPG-VP and LTE-T assumptions, the analysis over the steady state predicts a critical temperature ratio S_H significantly lower than that observed in simulations. Similarly, the growth rate of the CPG-CP remains negative, although a bifurcation is observed around $S \approx 0.0909$ with this model. Consequently, all the viscous heated jets studied here are found to undergo a subcritical bifurcation, similarly to the low-density jet experiments of Zhu *et al.* (2017).

For the cases presented in figure 10(*a*), differences in the inlet mass flow $\dot{m} = 2\int_0^{1.1R} 2\pi\rho w r \, dr$ due to the change of TTP models are likely to influence the global stability behaviour. However, no clear correlations between $\dot{m}$ and the growth rates were found, and it does not seem to be the dominant mechanism here.

In the local analyses, the absolute growth rates are found to decrease monotonically after the inlet in all cases, unlike in the study of Coenen & Sevilla (2012) where different trends were observed depending on the inlet profiles' shape. Figure 10(*b*) shows the lengths of the absolute regions as a function of S, normalized by the inlet absolute wavelength $\lambda_0 = 2\pi \text{Re}(\alpha)^{-1}$. The main difference between trends from the local and global analyses is observed with the LTE-T jets after $S \leq 0.1429$. While the global analysis correctly retrieves that this model remains unstable at low S, the local analysis suggests a restabilization similar to that of the LTE-h jets. A possible reason for this discrepancy is found by observing that the separation of scales between the development length of the flow L_{flow} (Huerre & Monkewitz 1990) and the typical wavelength of instabilities λ_0^* is no longer respected for these cases, as seen in figure 11(*a*). The same is observed for both LTE models, which is probably due to the faster spreading observed for these two base states.

Absolute instabilities in low-density jets are known to arise from the baroclinic torque $\Gamma = (\nabla\rho \times \nabla p)/\rho^2$ (Lesshafft & Huerre 2007), therefore, the velocity and density gradients from the base state profiles one diameter downstream of the inlet are investigated
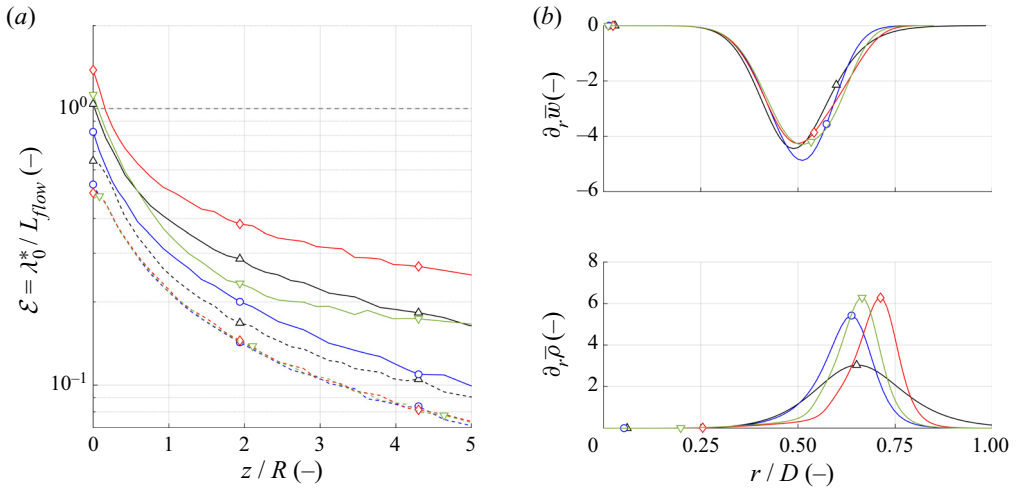
936 A7-17

Figure 11. Characteristics of the local linear analysis for the CPG-CP ($\triangle$), CPG-VP ($\circ$), LTE-h ($\diamond$) and LTE-T (∇) flow models: (*a*) criterion ε for the separation of scales between the development length of the flow and typical perturbation's wavelengths with $S = 0.0667$ (——) and $S = 0.2$ (- - -); (*b*) local base state radial gradients at $z = 1D$ for the $S = 0.1$ case.

in figure 11(*b*). To highlight the influence of the flow models, the case with $S = 0.1$ is plotted. In that case, the CPG-CP flow yields a density gradient $\partial_r \bar{\rho}$ approximately half as strong as for the other models, damping the absolute instability. As expected, the LTE-h model's density gradient is shifted outward from the shear layer, thus damping the baroclinic torque. This observation is coherent with previous analyses of parallel flows with the same TTP models (Demange & Pinna 2020), but its effect is stronger in the case of spatially developing flows as they experience a faster spreading in LTE, thus damping Γ.

4.2. *Influence of flow modelling on the global mode*

As seen in the previous sections, the TTP models affect the stability features of heated jets. However, deriving local and BiGlobal stability equations while taking into account detailed TTP models leads to long expressions, prone to derivation mistakes if not done automatically (Pinna 2013). In the following, different TTP models are used for the base state computations and in the stability problem, in order to decouple the influence of (i) the primary flow quantities coming from the base flow and (ii) the reconstructed secondary flow quantities in the perturbation equations, on the stability features. The goal of this analysis is to estimate at which point more complex stability equations become critical to the analysis of heated jets.

Results from this approach are presented in figure 12, where the isolated mode's growth rate is plotted for each base state and stability assumption, as a function of the temperature ratio S. For most of the range of S studied, and a large part of the range studied in the literature, trends of the growth rate are found to depend mainly on the choice of base state. More precisely, they depend on the influence of a given set of thermodynamic and transport properties on the development of the primary flow quantities (in our case $\boldsymbol{u}, T, p$) through the Navier–Stokes' equations. For example, the particular trend previously observed with the LTE-h jet is recovered with all stability models in figure 12(*b*).
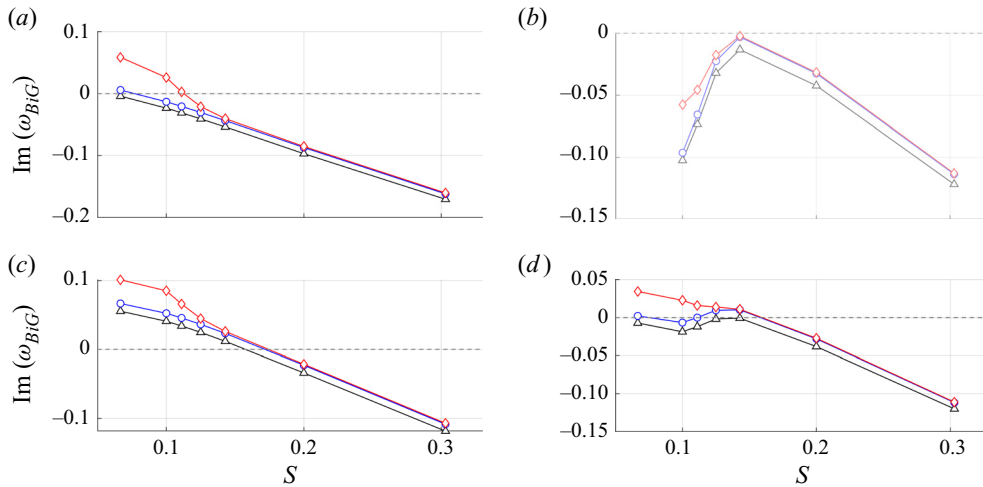
Figure 12. Comparison of the BiGlobal growth rates as a function of the temperature ratio S obtained while decoupling the TTP models from the base state and stability computations. Stability computations are performed assuming CPG-CP ($\triangle$), CPG-VP ($\circ$) and LTE ($\diamond$), while base states are computed assuming: (*a*) CPG-CP; (*b*) LTE-h; (*c*) CPG-VP; (*d*) LTE-T.

Nonetheless, some effects resulting from a change of TTP model in the stability problem and secondary flow quantities are also observed for the same base state. First, adding temperature-dependent transport properties to the CPG model is found to have a slight destabilizing effect on the global mode, similar in amplitude for all temperature ratios and base states. This is in agreement with the observation made by Coenen *et al.* (2017), that the drop of temperature-dependent viscosity in the shear layer and outer flow should result in an increase of the local effective Reynolds number, and is shown in figure 13(*a*) for the $S = 0.1$ CPG-VP jet.

For temperature ratios above $S \geq 0.125$, the CPG-VP and LTE stability models are found to give almost identical results, even though the threshold of vibrational excitation ($T_{vib} \approx 800\,\text{K}$, $S \approx 0.44$) is greatly exceeded. Therefore, no effects specific to the vibrational excitation and thus breakdown of the CPG assumption are observed on the linear stability, despite observations related to bifurcation parameters made from the DNS.

However, differences between the CPG and LTE assumptions gradually increase for $S < 0.125$ in all cases, after which the LTE model becomes significantly more unstable than the others for a given base state. In order to identify the underlying causes for the departure of the LTE results, the Reynolds number defined from the inlet mass flow, $Re_m = \dot{m}/(\pi R \mu_c)$, is plotted in figure 13(*b*) for the CPG-VP base state corresponding to the growth rates of figure 12(*c*). We observe that the destabilisation obtained with the LTE model can be correlated to an increase of the mass-flow Reynolds number for this TTP model. Furthermore, the threshold value of $S = 0.125$ is found to correspond quite accurately to the onset of the first dissociation reactions occurring in the equilibrium mixture as S decreases (see figure 1). Therefore, it appears that the change in gas composition resulting from the gas chemistry, combined with the imposed $Re = \rho_c w_c R/\mu_c = 200$, results in a modification of the bulk flow conditions, destabilizing the LTE global mode.

This last result agrees with the outcome of local analyses in parallel flows (Demange & Pinna 2020), observing that the LTE assumption is destabilizing when added to the stability equations, but often stabilizing when included in the base state computation (with respect to the CPG assumption). This is particularly important because the LTE
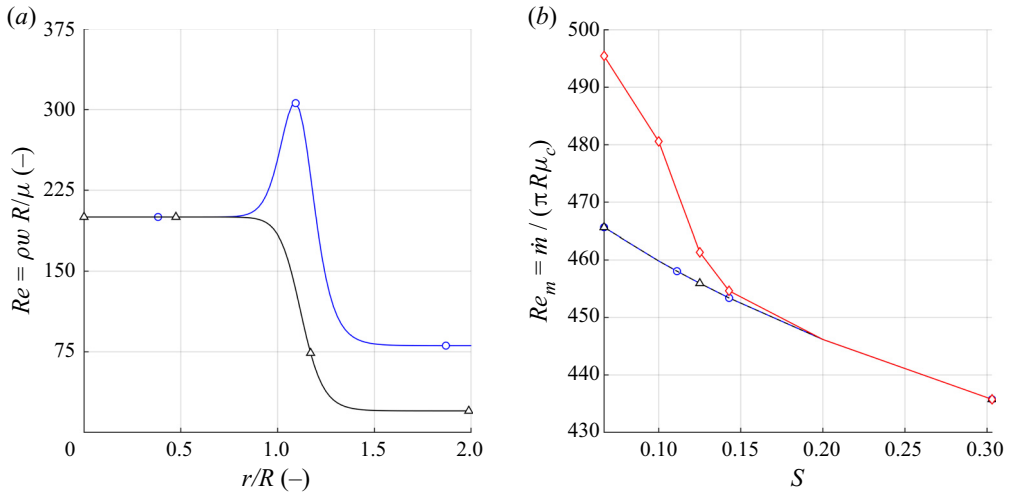
Figure 13. (*a*) Comparison of the local Reynolds number $Re = \rho w R/\mu$ obtained on the CPG-VP base state for $S = 0.1$ at $z = 1D$ when using the CPG-CV ($\triangle$) and CPG-VP ($\circ$) to rebuild secondary flow quantities (the non-zero Reynolds in the outer flow are due to the 1 % co-flow injected). (*b*) Comparison of the inlet mass-flow Reynolds numbers $Re_m = \dot{m}/(\pi R \mu_c)$ obtained when using the CPG-CP ($\triangle$), CPG-VP ($\circ$) and LTE ($\diamond$) models to rebuild secondary flow quantities on CPG-VP base states, corresponding to the growth rates of figure 12(*c*).

model is the most physically accurate assumption studied here for high temperatures ($T > T_{vib}$). These results show that the stability analysis requires accurate thermodynamic and transport models above the dissociation temperature, which corresponds to $T = 2800$ K for air at $p_s = 100$ mbar.

4.3. *Frequency prediction*

Figure 14 compares the real non-dimensional frequencies obtained from local (figure 14*a*) and global (figure 14*b*) linear analyses, against those obtained from the DNS. In agreement with well-known results (Lesshafft *et al.* 2007; Coenen & Sevilla 2012), the local linear stability approach makes it possible to satisfactorily predict the global mode frequency from the DNS in the vicinity of the bifurcation. However, as S decreases, the error in the frequency becomes as large as respectively 115 % and 41 % for the LTE-T and CPG-VP jets at $S = 0.0667$. Interestingly, using the BiGlobal approach on steady states only marginally improves the frequency prediction. For the highest values of S, the linear global and local absolute frequencies are in excellent agreement, with relative discrepancies of the order of 1 %. When decreasing S, the local and global approaches diverge from each other, in particular for the LTE-T jets where non-parallel effects were previously found to be stronger than for CPG jets. The present frequency observations confirm that the linear analyses performed on steady states are only relevant to describe instabilities around a fixed point, while nonlinear analyses are required to capture the behaviour around a limit cycle observed in the viscous unsteady simulations.

5. BiGlobal analysis of the mean flows

As seen in the previous section, the highly viscous heated jets studied in this study undergo a subcritical Hopf bifurcation, with the onset of the global nonlinear mode occurring before the flow becomes linearly (and globally) unstable. Consequently, the
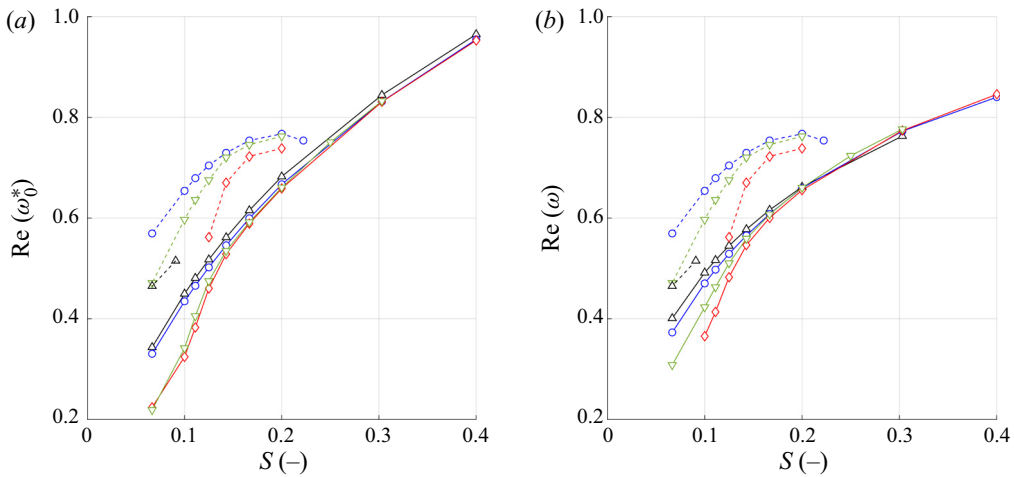
Figure 14. Frequency behaviour of the heated jets retrieved from linear analyses of the steady states (——) with the CPG-CP ($\triangle$), CPG-VP ($\circ$), LTE-h ($\diamond$) and LTE-T ($\triangledown$) flow models, compared against the frequencies from the FFT analysis (- - -): (*a*) absolute inlet frequency from the local analysis; (*b*) real frequency from the BiGlobal problem.

agreement between linear mode frequencies and DNS observations quickly degrade as the temperature ratio is lowered below that of the bifurcation S_H.

In this context, linear BiGlobal analyses are performed on the time-averaged state $\hat{q}$, obtained from the unsteady simulations, rather than on the steady state $\bar{q}$. This type of analysis was performed in the literature for the flow past cylinders (Sipp & Lebedev 2007; Leontini, Thompson & Hourigan 2010), showing that under specific conditions discussed in their paper, this type of analysis could closely match frequencies of flows in the limit cycle. Similar methodologies were also successfully applied to convectively unstable jets, using experimental (Oberleithner, Rukes & Soria 2014) and numerical (Tammisola & Juniper 2016) unsteady flows to obtain an average state. In the present case, however, criteria for the validity of the mean flow analysis are not computed, but the results are evaluated by comparing them with data from unsteady simulations.

For each setting, the range of iterations considered to compute the average state begins after the transient phase, so as to consider only the periodic flow regime. Similarly, in cases where secondary vortices were ejected out of the jets, the iterations considered start after the dissipation of these structures. Comparisons of the steady state against the mean state are displayed in figure 15(*a*), and show that density fields are particularly affected by this change. From the inlet to about one diameter downstream, steady and average states are almost identical, which renders the computation of the inlet absolute frequency on the average state unnecessary. Further downstream, the average flow's density layer undergoes a sudden shift outward from that of the steady flow, which is expected to influence the baroclinic torque. Similar observations are made for all cases and models, but are particularly present near the bifurcation S_H and eventually reduce as S is further lowered.

The linear BiGlobal analyses on the averaged states yield eigenvalue spectra with a similar structure to those obtained on the steady base state, as illustrated in figure 15(*b*). Most notable changes are observed for the isolated mode, both in terms of growth rate and real frequency, while modes near the origin are hardly affected.
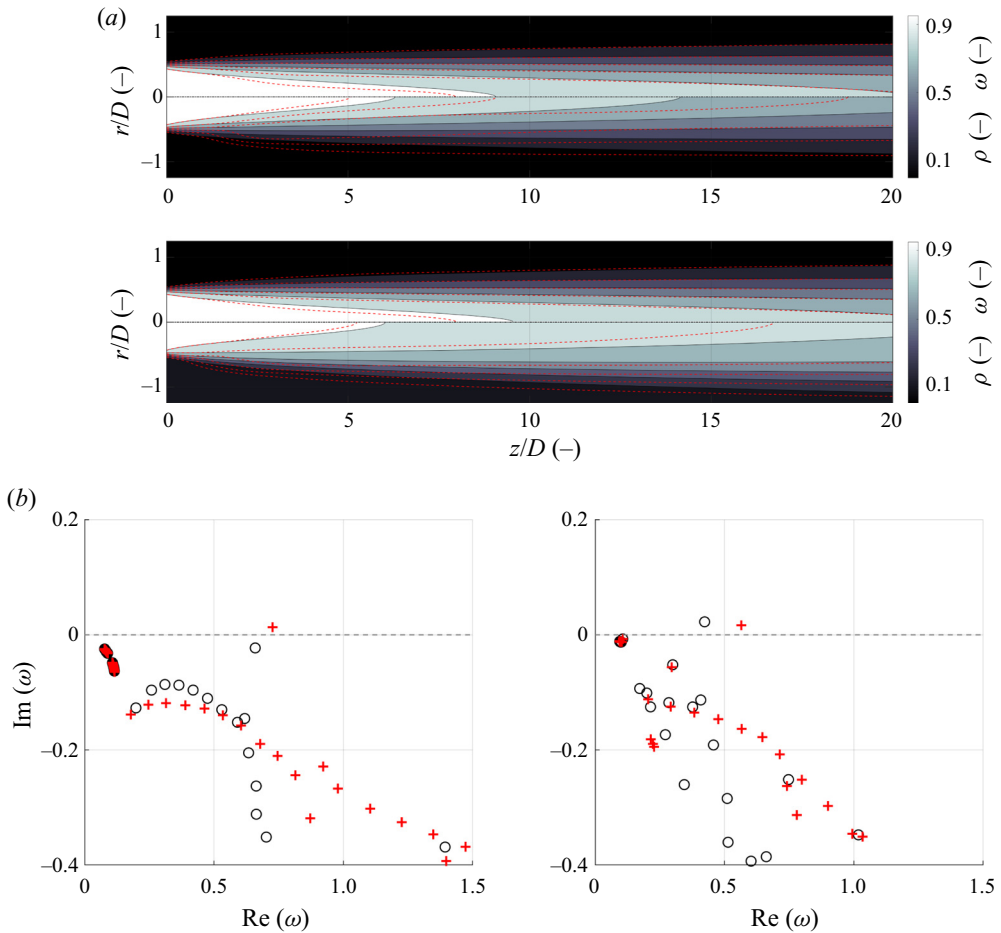
Figure 15. Comparisons of the base states and stability features obtained from the steady and average flows: (*a*) displays contours of the streamwise velocity (upper halves) and density (bottom halves) obtained from the steady (——) and averaged (- - -) flows, for the CPG-VP case with $S = 0.2$ (up) and the LTE-T case with $S = 0.1$ (bottom); (*b*) displays examples of the global eigenvalue spectra obtained for the same cases (left: CPG-VP; right: LTE-T) using the steady ($\circ$) and average ($+$) flow as base states.

5.1. *Mode shapes and baroclinic torque*

Before addressing the topic of frequency estimation, we evaluate the ability of the present analysis to capture stability features observed in the unsteady simulations. First, the baroclinic torque $\Gamma = (\nabla \rho \times \nabla p)/\rho^2$ from the DNS is computed for a snapshot of the instantaneous flow fields obtained during the simulations. Second, the BiGlobal mode perturbations q' computed on the time-averaged state are used to obtain an alternative instantaneous flow field $q^* = \hat{q} + \nu q'$, where ν is a real factor chosen to reproduce the amplitude of the perturbations observed in the DNS. For convenience, $t = 1$ is imposed in the complex phase function $\phi = -i\omega t$ of q'. Third, the same procedure as for the instantaneous DNS fields is used to obtain the baroclinic torque associated with q^*.

Examples of the reconstructed baroclinic torque are given in figure 16 for three cases including that of figure 15. In order to complete the comparison, the same term obtained from the global mode on the steady states is added in a similar fashion. As a result, the quality of the comparisons between shapes of the baroclinic torque is found to
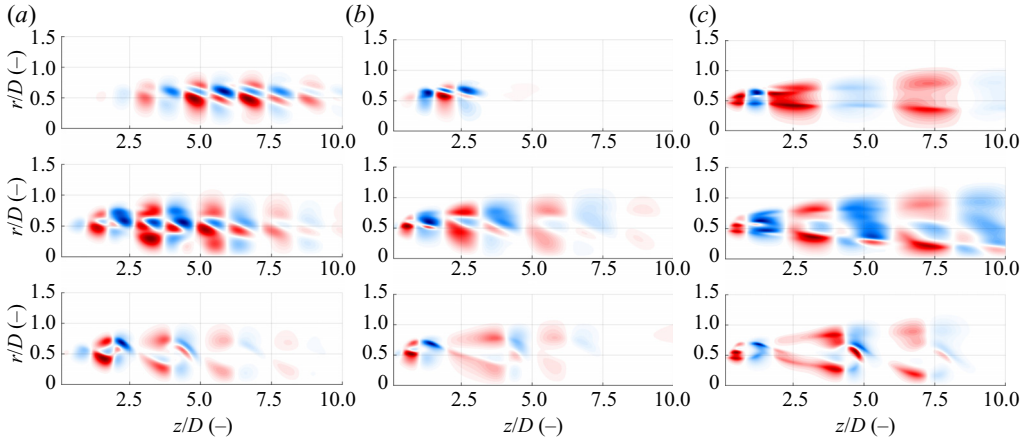
Figure 16. Comparison of the baroclinic torque $\Gamma = (\nabla \rho \times \nabla p)/\rho^2$ obtained from the global mode over the steady state (up), the global mode over the time-average state (middle) and the instantaneous DNS fields (bottom), for (*a*) the CPG-VP jet with $S = 0.2$; (*b*) the LTE-T jet with $S = 0.1$ which exhibit vortex coupling; and (*c*) the LTE-T jet with $S = 0.0667$ which produces pairs of closely travelling vortices. Figures present a zoomed-in portion of the numerical domains. For each case, the animations corresponding to the baroclinic torque from the DNS can be found in the supplementary materials (movie_3a, movie_3b and movie_3c).

depend on both the TTP model, and whether or not vortex coupling was observed in the corresponding simulations.

In the absence of vortex coupling (see figure 16*a*), the linear analysis over time-averaged states reproduces the baroclinic torque observed in the DNS for the first diameters ($z \leq 5D$) after the inlet. In this region, both the shapes and spatial wavelength of the instabilities are well captured. However, the comparison degrades somewhat further downstream as the baroclinic torque from the DNS instantaneous fields vanishes before that of the BiGlobal mode along z. In the case of the global modes over the steady, but unstable, base flow, the baroclinic torque differs significantly from those observed in the DNS. This is because the oscillations in the DNS have a large amplitude and the flow cannot be well represented by a small perturbation developing on a steady base flow.

In LTE-T jets in which strong interactions are observed between vortical structures, the agreement between linear analyses over the time-averaged state and the DNS is limited to an even shorter region after the inlet. Further downstream, the vortex coupling events and proximity between structures strongly alters the shape of the DNS baroclinic torque, which is not captured by the linear analyses. These observation are done whether vortices undergo a coupling event (figure 16*b*), or travel in close pairs ($S = 0.0667$ in figure 16*c*).

5.2. *Frequency matching*

The frequencies obtained from the linear analysis on the averaged states are compared against the FFT ones from the DNS in figure 17. Overall, the linear analyses on $\hat{q}$ are in significantly better agreement with the simulations than those on $\bar{q}$. For both the CPG-VP and LTE-h jets, the nonlinear frequency is retrieved with a 5 % discrepancy for the whole range of temperature ratios studied. In the LTE-T cases with strong vortex interactions ($S \leq 0.1$), the agreement between the frequency from stability analysis and the DNS deteriorates, with an error of the order of 15 % for $S = 0.0667$. This disagreement is coherent with the analysis of the baroclinic torque shape for the same LTE-T cases.
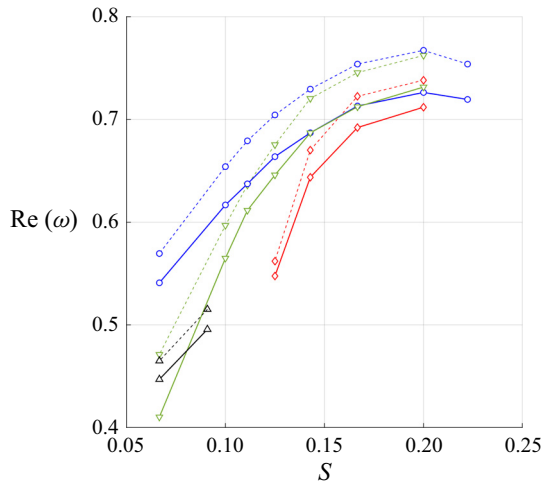
Figure 17. Comparison of the real non-dimensional frequencies obtained from the FFT analyses on unsteady simulations ($\cdots$) against that of the BiGlobal analyses on the time-averaged states (——) for the different flow models: CPG-CP ($\triangle$), CPG-VP ($\circ$), LTE-h ($\diamond$) and LTE-T ($\triangledown$).

Despite coupling events, the frequency of the CPG-VP jet with $S = 0.0667$ is well captured by the linear analysis on the averaged state, within 5 %.

6. Conclusions

The stability features of viscous heated air jets have been investigated for a Reynolds number of 400 and relatively thin inlet shear layers ($R/\theta = 20$), while varying the temperature ratio between $0.0667 \leq S \leq 0.4$. In addition, the influence of different thermodynamic, transport and gas chemical properties on the dynamic behaviour of the jets was evaluated by means of unsteady axisymmetric simulations and linear stability analyses (local and Biglobal). To the authors' knowledge, this work is the first to explore such low temperature ratios and to include high-enthalpy flow models in the global stability analysis of heated jets.

The first result of this study is that accurate modelling of the transport and thermodynamic properties of the fluid proved to be paramount in capturing the dynamic behaviour of heated jets, depending on the parameters studied. In unsteady simulations the introduction of a temperature-dependent viscosity law is enough to roughly double the bifurcation temperature ratio with respect to a constant viscosity case. With the appearance of dissociation reactions ($T_{diss} \approx 2800$ K and $S_{diss} \approx 0.125$ for air at $p_s = 100$ mbar), simulations reveal increasingly different dynamic behaviours for gases with (LTE) and without (CPG) active chemistry, with differences in oscillation frequencies up to 20 %. Furthermore, results show that for gases in LTE, changes to the formulation of the inlet energy condition can radically alter the behaviour of the flow.

Local and global linear stability analyses of the corresponding steady states were performed to investigate the differences in behaviours observed between different flow models. For centreline temperatures below that of dissociation reactions, the different flow assumptions affect the global growth rate mainly through changes of the base state spatial structure and resulting baroclinic torque. Thus, high-enthalpy effects can be omitted from the stability equations. On the other hand, the LTE stability equations predict a significantly larger growth rate than their CPG counterpart on the same base state

for $S \leq S_{diss}$. This destabilization of the LTE global mode was found to be correlated with an increase of the mass-flow averaged Reynolds number at the inlet, induced by the change of density of the dissociated mixture. However, these analyses return only a qualitative description of the dynamic behaviour of the jets. In agreement with the literature (Lesshafft *et al.* 2007; Coenen & Sevilla 2012), the absolute frequency predicts the oscillations frequency at the bifurcation, but diverges for lower S. Similar results are obtained from the global analysis. For each TTP model, the onset of self-sustained oscillations in the DNS occurs at higher S than the global linear instability threshold. A possible reason for this subcritical bifurcation may lie in a strong non-normality of the linear operator for the cases studied, increasing the sensitivity of the flow to noise and transient growth (Chomaz 2005). However, the adjoint or nonlinear front analyses would be required to inspect the nonlinearity and such present cases lie beyond the scope of this paper.

Finally, a global linear analysis was performed over the time-averaged states obtained from unsteady simulations of the globally unstable jets, similarly to previous analyses of flows in limit cycles (Sipp & Lebedev 2007; Leontini *et al.* 2010; Oberleithner *et al.* 2014; Turton, Tuckerman & Barkley 2015; Tammisola & Juniper 2016). Although no criterion supporting the validity of this approach was inspected, in most cases, the frequencies obtained were found in remarkably good agreement with those observed in the DNS. Furthermore, by using the modes based on the averaged state, this analysis was able to reproduce the shape of the baroclinic torque predicted by the DNS. Therefore, viscous heated jets undergoing subcritical bifurcation could belong to the category of flows for which the mean flow analysis yields meaningful results, which is not always the case (Sipp & Lebedev 2007; Turton *et al.* 2015).

Author ORCIDs.
- S. Demange https://orcid.org/0000-0002-3638-4988;
- U.A. Qadri https://orcid.org/0000-0003-1360-6223;
- M.P. Juniper https://orcid.org/0000-0002-8742-9541.

Appendix A. Details of the linear stability computations

This section gives further details on the numerical stability problems solved in this paper. In the following, spatial and thermodynamic derivatives use a compact notation (e.g. $\partial_T \bar{q} \rightarrow \bar{q}_T$ and $\partial_T^2 \bar{q} \rightarrow \bar{q}_{TT}$) for convenience.

A.1. *Perturbations of secondary quantities*

Unlike the method proposed by Coenen & Sevilla (2012), the eigenvector appearing in the EVP of (2.13) is defined only for the primary quantities $\tilde{q} = [\tilde{\boldsymbol{u}}, \tilde{T}, \tilde{p}]$, while primary quantities are substituted using the first-order terms (for the linear stability theory) of a

Taylor expansion (Pinna 2012), such that for a secondary quantity 'q_d',

$$q_d(\boldsymbol{x}, t) = \bar{q}_d(\boldsymbol{x}) + \underbrace{\sum_{n=1}^{2} \frac{\partial \overline{q_d}(\boldsymbol{x})}{\partial \overline{q_n}(\boldsymbol{x})} q_n'(\boldsymbol{x}, t)}_{q_d'}, \tag{A1}$$

where the two primary thermodynamic quantities from table 1 are labelled as q_n, $n \in [1, 2]$, and thermodynamic derivatives of the secondary quantities are obtained analytically from the property models in VESTA (Miró Miró 2020, Section 8.2). Furthermore, spatial derivatives of secondary perturbations are obtained using a chain rule during the derivation of the stability equations

$$\frac{\partial q_d'}{\partial x^i} = \sum_{n=1}^{2} \left[\frac{\partial}{\partial x^i} \left(\frac{\partial \bar{q}_d}{\partial \bar{q}_n} \right) q_n' + \frac{\partial \bar{q}_d}{\partial \bar{q}_n} \frac{\partial q_n'}{\partial x^i} \right], \tag{A2}$$

where the first term in the summation is also obtained with the chain rule

$$\frac{\partial}{\partial x^i} \left(\frac{\partial \bar{q}_d}{\partial \bar{q}_n} \right) = \sum_{m=1}^{2} \frac{\partial^2 \bar{q}_d}{\partial \bar{q}_n \partial \bar{q}_m} \frac{\partial \bar{q}_m}{\partial x^i}, \tag{A3}$$

which avoids the computation of numerical spatial derivatives, but requires higher order of the thermodynamic analytical derivatives, provided in VESTA for the flow models discussed in this study.

A.2. *Boundary conditions for perturbation equations*

Within the local analysis, computational domains are extended up to $r_{max} = 35R$ away from the centreline. One-dimensional perturbations are assumed to vanish in the outer flow $\lim_{r \to \infty} \tilde{q} = 0$, while a set of centreline boundary conditions from a previous study (Demange & Pinna 2020) are applied at $r = 0$. Assuming axisymmetric perturbations, the conditions are given as

$$\tilde{u} = \tilde{v} = 0, \tag{A4a}$$

$$\tilde{w}_r = \tilde{T}_w = 0, \tag{A4b}$$

$$i\alpha\tilde{w} + 2\tilde{u}_r - (i\omega - i\alpha\bar{w}) \left(\frac{\bar{F}\tilde{p}}{\bar{P}} - \frac{\bar{G}\tilde{T}}{\bar{T}} \right) = 0, \tag{A4c}$$

within the LTE assumption. Calorically perfect gas conditions are retrieved by setting $\bar{\zeta} = \bar{F} = \bar{G} = 1$.

For the BiGlobal problem, centreline boundary conditions are obtained with the same method as for the local problem, while neglecting the base radial velocity component $\bar{u} \ll \bar{w}$. This leads to the same centreline boundary conditions as (A 4a) and (A 4b), with

the exception of (A 4c) which is replaced by

$$
\bar{F}\bar{w}\tilde{p}_z - \frac{\bar{w}\bar{\zeta}_{\bar{p}\bar{p}}\bar{p}\bar{p}_z\tilde{p}}{\bar{\zeta}} + \frac{2\bar{w}\left(\bar{\zeta}_{\bar{p}}\right)^2\bar{p}\bar{p}_z\tilde{p}}{\bar{\zeta}^2} - \frac{2\bar{w}\bar{\zeta}_{\bar{p}}\bar{p}_z\tilde{p}}{\bar{\zeta}}
$$

$$
+ \frac{2\bar{T}_z\bar{w}\bar{\zeta}_{\bar{T}}\bar{\zeta}_{\bar{p}}\bar{p}\tilde{p}}{\bar{\zeta}^2} + \frac{\bar{T}_z\bar{w}\bar{\zeta}_{\bar{p}}\bar{p}\tilde{p}}{\bar{T}\bar{\zeta}} - \frac{\bar{T}_z\bar{w}\bar{\zeta}_{\bar{T}\bar{p}}\bar{p}\tilde{p}}{\bar{\zeta}} - \mathrm{i}\bar{F}\omega\tilde{p}
$$

$$
- \frac{\bar{T}_z\bar{w}\bar{\zeta}_{\bar{T}}\tilde{p}}{\bar{\zeta}} + \bar{F}\bar{w}_z\tilde{p} - \frac{\bar{T}_z\bar{w}\tilde{p}}{\bar{T}} + \frac{2\tilde{T}\bar{w}\bar{\zeta}_{\bar{T}}\bar{\zeta}_{\bar{p}}\bar{p}\bar{p}_z}{\bar{\zeta}^2} + \frac{\tilde{T}\bar{w}\bar{\zeta}_{\bar{p}}\bar{p}\bar{p}_z}{\bar{T}\bar{\zeta}}
$$

$$
- \frac{\tilde{T}\bar{w}\bar{\zeta}_{\bar{T}\bar{p}}\bar{p}\bar{p}_z}{\bar{\zeta}} - \frac{\tilde{T}\bar{w}\bar{\zeta}_{\bar{T}}\bar{p}_z}{\bar{\zeta}} + \bar{F}\tilde{w}\tilde{p}_z - \frac{\tilde{T}\bar{w}\bar{p}_z}{\bar{T}} + \frac{\mathrm{i}\bar{G}\tilde{T}\omega\bar{p}}{\bar{T}}
$$

$$
- \frac{\bar{T}_z\tilde{T}\bar{w}\bar{\zeta}_{\bar{T}\bar{T}}\bar{p}}{\bar{\zeta}} + \frac{2\bar{T}_z\tilde{T}\bar{w}\left(\bar{\zeta}_{\bar{T}}\right)^2\bar{p}}{\bar{\zeta}^2} + \frac{2\bar{T}_z\tilde{T}\bar{w}\bar{\zeta}_{\bar{T}}\bar{p}}{\bar{T}\bar{\zeta}} + \tilde{w}_z\bar{p}
$$

$$
- \frac{\bar{G}\bar{T}_z\tilde{w}\bar{p}}{\bar{T}} - \frac{\bar{G}\tilde{T}\bar{w}_z\bar{p}}{\bar{T}} - \frac{\bar{G}\tilde{T}_z\bar{w}\bar{p}}{\bar{T}} + \frac{2\bar{T}_z\tilde{T}\bar{w}\bar{p}}{\bar{T}^2} + 2\tilde{u}_r\bar{p} = 0. \tag{A5}
$$

Due to its two-dimensional perturbations $\tilde{q}$, the BiGlobal problem also requires boundary conditions at the inlet $(r = 0)$, lateral $(r = r_{\max})$ and outlet $(z = z_{\max})$ edges of the domain. A no-stress condition is applied to the lateral and outlet edges: $(p'\delta_{ij} + \tau'_{ij}) \cdot \boldsymbol{n} = 0$. For the lateral condition, $\boldsymbol{n} = \bar{e}_r$, resulting in three equations

$$
-\frac{\bar{u}\bar{\lambda}_{\bar{p}}\tilde{p}}{Re\,r} - \frac{\tilde{T}\bar{u}\bar{\lambda}_{\bar{T}}}{Re\,r} - \frac{\mathrm{i}\tilde{v}\beta\bar{\lambda}}{Re\,r} - \frac{\tilde{u}\bar{\lambda}}{Re\,r} - \frac{2\bar{u}_r\bar{\mu}_{\bar{p}}\tilde{p}}{Re} - \frac{\bar{w}_z\bar{\lambda}_{\bar{p}}\tilde{p}}{Re} - \frac{\bar{u}_r\bar{\lambda}_{\bar{p}}\tilde{p}}{Re}
$$

$$
+\tilde{p} - \frac{2\tilde{T}\bar{u}_r\bar{\mu}_{\bar{T}}}{Re} - \frac{2\tilde{u}_r\bar{\mu}}{Re} - \frac{\tilde{T}\bar{w}_z\bar{\lambda}_{\bar{T}}}{Re} - \frac{\tilde{T}\bar{u}_r\bar{\lambda}_{\bar{T}}}{Re} - \frac{\tilde{w}_z\bar{\lambda}}{Re} - \frac{\tilde{u}_r\bar{\lambda}}{Re} = 0, \tag{A6a}
$$

$$
\frac{\bar{v}\bar{\mu}_{\bar{p}}\tilde{p}}{Re\,r} + \frac{\tilde{T}\bar{v}\bar{\mu}_{\bar{T}}}{Re\,r} - \frac{\mathrm{i}\tilde{u}\beta\bar{\mu}}{Re\,r} + \frac{\tilde{v}\bar{\mu}}{Re\,r} - \frac{\bar{v}_r\bar{\mu}_{\bar{p}}\tilde{p}}{Re} - \frac{\tilde{T}\bar{v}_r\bar{\mu}_{\bar{T}}}{Re} - \frac{\tilde{v}_r\bar{\mu}}{Re} = 0, \tag{A6b}
$$

$$
-\frac{\bar{w}_r\bar{\mu}_{\bar{p}}\tilde{p}}{Re} - \frac{\bar{u}_z\bar{\mu}_{\bar{p}}\tilde{p}}{Re} - \frac{\tilde{T}\bar{w}_r\bar{\mu}_{\bar{T}}}{Re} - \frac{\tilde{T}\bar{u}_z\bar{\mu}_{\bar{T}}}{Re} - \frac{\tilde{w}_r\bar{\mu}}{Re} - \frac{\tilde{u}_z\bar{\mu}}{Re} = 0, \tag{A6c}
$$

with $\bar{\lambda} = -2/3\bar{\mu}$, completed by $\tilde{T} = 0$ and the linearized continuity equation at the boundary. At the outlet, $\partial_z\tilde{T} = 0$ and the linearized continuity equation complete the no-stress boundary conditions. At the inlet, a Dirichlet condition is applied to all perturbations, except for $\partial_z\tilde{p} = 0$.

REFERENCES

ÅKERVIK, E., BRANDT, L., HENNINGSON, D.S., HÆPFFNER, J., MARXEN, O. & SCHLATTER, P. 2006 Steady solutions of the Navier–Stokes equations by selective frequency damping. *Phys. Fluids* **18** (6), 068102.

ANDERSON, J.D. 2006 *Hypersonic and High-Temperature Gas Dynamics*, 3rd edn. American Institute of Aeronautics and Astronautics.

BALESTRA, G. 2013 Spatio-temporal linear stability analysis for heated coaxial jet flows. Master's thesis, ETH Zurich.

BALESTRA, G., GLOOR, M. & KLEISER, L. 2015 Absolute and convective instabilities of heated coaxial jet flow. *Phys. Fluids* **27** (5), 054101.

BERS, A. 1984 Space-time evolution of plasma instabilities-absolute and convective. In *Basic Plasma Physics*, p. 451. Cambridge University Press.

BHARADWAJ, K.K. & DAS, D. 2017 Global instability analysis and experiments on buoyant plumes. *J. Fluid Mech.* **832**, 97–145.

BHARADWAJ, K.K. & DAS, D. 2019 Puffing in planar buoyant plumes: BiGlobal instability analysis and experiments. *J. Fluid Mech.* **863**, 817–849.

BRIGGS, R.J. 1964 *Electron-Stream Interaction with Plasmas*. MIT Press.

CHAKRAVARTHY, R.V.K., LESSHAFFT, L. & HUERRE, P. 2018 Global stability of buoyant jets and plumes. *J. Fluid Mech.* **835**, 654–673.

CHANDLER, G.J., JUNIPER, M.P., NICHOLS, J.W. & SCHMID, P.J. 2012 Adjoint algorithms for the Navier–Stokes equations in the low Mach number limit. *J. Comput. Phys.* **231** (4), 1900–1916.

CHOMAZ, J. 2005 Global instabilities in spatially developing flows: non-normality and nonlinearity. *Annu. Rev. Fluid Mech.* **37**, 357–392.

CHOMAZ, J.M., HUERRE, P. & REDEKOPP, L.G. 1988 Bifurcations to local and global modes in spatially developing flows. *Phys. Rev. Lett.* **60** (1), 25–28.

CIPULLO, A. 2010 Plasma flow characterisation by means of optical emission diagnostics. *Project Rep.* 2010-05. von Kármán Institute, Rhode Saint Genèse, Belgium.

CIPULLO, A., HELBER, B., PANERAI, F., ZENI, F. & CHAZOT, O. 2014 Investigation of freestream plasma flow produced by inductively coupled plasma wind tunnel. *J. Thermophys. Heat Transfer* **28** (3), 381–393.

COENEN, W., LESSHAFFT, L., GARNAUD, X. & SECILLA, A. 2017 Global instability of low-density jets. *J. Fluid Mech.* **820**, 187–2017.

COENEN, W. & SEVILLA, A. 2012 The structure of the absolutely unstable regions in the near field of low-density jets. *J. Fluid Mech.* **713**, 123–149.

COENEN, W., SEVILLA, A. & SANCHEZ, A.L. 2008 Absolute instability of light jets emerging from circular injector tubes. *Phys. Fluids* **20**, 074104.

COUAIRON, A. & CHOMAZ, J.-M. 1999 Fully nonlinear global modes in slowly varying flows. *Phys. Fluids* **11** (12), 3688–3703.

DEMANGE, S., CHAZOT, O. & PINNA, F. 2020 Local analysis of absolute instability in plasma jets. *J. Fluid Mech.* **903**, 124104.

DEMANGE, S. & PINNA, F. 2020 On the role of thermo-transport properties in the convective/absolute transition of heated round jets. *Phys. Fluids* **32** (12), 124104.

DEMANGE, S., QADRI, U.A. & PINNA, F. 2019 Linear impulse response of a plasma jet. In *Proceedings of the IUTAM Symposium on Laminar Turbulent Transition* (ed. S. Sherwin, P. Schmid & X. Wu). Springer.

HALLBERG, M.P. & STRYKOWSKI, P.J. 2006 On the universality of global modes in low-density axisymmetric jets. *J. Fluid Mech.* **569**, 493–507.

HERMANNS, M. & HERNÁNDEZ, J.A. 2008 Stable high-order finite-difference methods based on non-uniform grid point distributions. *Intl J. Numer. Meth. Fluids* **56** (3), 233–255.

HUERRE, P. 2000 Open shear flow instabilities. In *Perspectives in Fluid Dynamics* (ed. G.K. Batchelor, H.K. Moffatt & M.G. Worster), pp. 159–229. Cambridge University Press.

HUERRE, P. & MONKEWITZ, P.A. 1985 Absolute and convective instabilities in free shear layers. *J. Fluid Mech.* **159**, 151–168.

HUERRE, P. & MONKEWITZ, P.A. 1990 Local and global instabilities in spatially developing flows. *Annu. Rev. Fluid Mech.* **22** (1), 473–537.

JENDOUBI, S. & STRYKOWSKI, P.J. 1994 Absolute and convective instability of axisymmetric jets with external flow. *Phys. Fluids* **6** (9), 3000–3009.

JUNIPER, M.J. 2006 The effect of confinement on the stability of two-dimensional shear flows. *J. Fluid Mech.* **565**, 171–195.

JUNIPER, M.J. 2008 The effect of confinement on the stability of non-swirling round jet/wake flows. *J. Fluid Mech.* **605**, 227–252.

KOLB, J.F., MOHAMED, A.-A.H., PRICE, R.O., SWANSON, R.J., BOWMAN, A., CHIAVARINI, R.L., STACEY, M. & SCHOENBACH, K.H. 2008 Cold atmospheric pressure air plasma jet for medical applications. *Appl. Phys. Lett.* **92** (24), 241501.

KYLE, D.M. & SREENIVASAN, K.R. 1993 The instability and breakdown of a round variable-density jet. *J. Fluid Mech.* **249** (1), 619–664.

LEONTINI, J.S., THOMPSON, M.C. & HOURIGAN, K. 2010 A numerical study of global frequency selection in the time-mean wake of a circular cylinder. *J. Fluid Mech.* **645**, 435–446.

LESSHAFFT, L. 2018 Artificial eigenmodes in truncated flow domains. *Theor. Comput. Fluid Dyn.* **32** (3), 245–262.

LESSHAFFT, L., COENEN, W., GARNAUD, X. & SEVILLA, A. 2015 Modal instability analysis of light jets. *Proc. IUTAM* **14**, 137–140.

LESSHAFFT, L. & HUERRE, P. 2007 Linear impulse response in hot round jets. *Phys. Fluids* **19** (2), 024102.

LESSHAFFT, L., HUERRE, P. & SAGAUT, P. 2007 Frequency selection in globally unstable round jets. *Phys. Fluids* **19**, 054108.

LESSHAFFT, L., HUERRE, P., SAGAUT, P. & TERRACOL, M. 2005 Global modes in hot jets, absolute/convective instabilities and acoustic feedback. In *11th AIAA/CEAS Aeroacoustics Conference*. American Institute of Aeronautics and Astronautics.

LESSHAFFT, L. & MARQUET, O. 2010 Optimal velocity and density profiles for the onset of absolute instability in jets. *J. Fluid Mech.* **662**, 398–408.

MALIK, M.R. & ANDERSON, E.C. 1991 Real gas effects on hypersonic boundary-layer stability. *Phys. Fluids* **3**, 803–821.

MARIEUA, V., REYNIERB, P., MARRAFFAB, L., VENNEMANNB, D., FILIPPISC, F.D. & CARISTIAC, S. 2007 Evaluation of scirocco plasma wind-tunnel capabilities for entry simulations in co2 atmospheres. *Acta Astronaut.* **61**, 604–616.

MICHALKE, A. 1984 Survey on jet instability theory. *Prog. Aerosp. Sci.* **21**, 159–199.

MIRÓ MIRÓ, F. 2020 Numerical investigation of hypersonic boundary-layer stability and transition in the presence of ablation phenomena. PhD Thesis, Universite Libre de Bruxelles/von Kármán Institute for Fluid Dynamics, Brussels, Belgium.

MIRÓ MIRÓ, F., BEYAK, E.S., PINNA, F. & REED, H.L. 2019 High-enthalpy models for boundary-layer stability and transition. *Phys. Fluids* **31** (4), 044101.

MONKEWITZ, P., BECHERT, D., BARSIKOW, B. & LEHMANN, B. 1990 Self-excited oscillations and mixing in a heated round jet. *J. Fluid Mech.* **213**, 611–639.

MONKEWITZ, P. & SOHN, K. 1998 Absolute instability in hot jets. *AIAA J.* **26**, 911–916.

NICHOLS, J. 2005 Simulation and stability analysis of jet diffusion flames. PhD thesis, University of Washington.

NICHOLS, J.W., SCHMID, P. & RILEY, J.J. 2007 Self-sustained oscillations in variable-density round jets. *J. Fluid Mech.* **582**, 341–376.

OBERLEITHNER, K., RUKES, L. & SORIA, J. 2014 Mean flow stability analysis of oscillating jet experiments. *J. Fluid Mech.* **757**, 1–32.

PARK, C. 1993 Review of chemical-kinetic problems of future NASA missions. I - Earth entries. *J. Thermophys. Heat Transfer* **7** (3), 385–398.

PINNA, F. 2012 Numerical study of stability for flows from low to high mach number. PhD thesis, Universita 'La Sapienza' di Roma/von Kármán Institute.

PINNA, F. 2013 VESTA toolkit: a software to compute transition and stability of boundary layers. In *43rd Fluid Dynamics Conference*. American Institute of Aeronautics and Astronautics.

QADRI, U.A., CHANDLER, G.J. & JUNIPER, M.P. 2015 Self-sustained hydrodynamic oscillations in lifted jet diffusion flames: origin and control. *J. Fluid Mech.* **775**, 201–222.

QADRI, U.A., CHANDLER, G.J. & JUNIPER, M.P. 2018 Passive control of global instability in low-density jets. *Eur. J. Mech.* B/*Fluids* **72**, 311–319.

SEVILLA, A., GORDILLO, J.M. & MARTÍNNEZ-BAZAN, C. 2002 The effect of the diameter ratio on the absolute and convective instability of free coflowing jets. *Phys. Fluids* **14** (9), 3028–3038.

SIPP, D. & LEBEDEV, A. 2007 Global stability of base and mean flows: a general approach and its applications to cylinder and open cavity flows. *J. Fluid Mech.* **593**, 333–358.

SPORES, R. & PFENDER, E. 1989 Flow structure of a turbulent thermal plasma jet. *Surf. Coat. Technol.* **37** (3), 251–270.

SREENIVASAN, K.R., RAGHU, S. & KYLE, D. 1989 Absolute instability in variable density round jets. *Exp. Fluids* **7** (5), 309–317.

SUTHERLAND, W. 1893 The viscosity of gases and molecular force. *Lond. Edinb. Dub. Phil. Mag. J. Sci.* **36** (223), 507–531.

TAMMISOLA, O. & JUNIPER, M.P. 2016 Coherent structures in a swirl injector at $Re = 4800$ by nonlinear simulations and linear global modes. *J. Fluid Mech.* **792**, 620–657.

THEOFILIS, V. 2003 Advances in global linear instability analysis of nonparallel and three-dimensional flows. *Prog. Aerosp. Sci.* **39** (4), 249–315.

TURTON, S.E., TUCKERMAN, L.S. & BARKLEY, D. 2015 Prediction of frequencies in thermosolutal convection from mean flows. *Phys. Rev.* E **91** (4), 043009.

ZHU, Y., GUPTA, V. & LI, L.K.B. 2017 Onset of global instability in low-density jets. *J. Fluid Mech.* **828**, R1.